J. Math. Biol. 46, 191–224 (2003)
Digital Object Identifier (DOI):
10.1007/s00285-002-0174-6

Mathematical Biology

Vittorio Cristini · John Lowengrub · Qing Nie

Nonlinear simulation of tumor growth

Received: 1 May 2002 / Revised version: 26 August 2002 /
Published online: 18 December 2002 – © Springer-Verlag 2002

Abstract. We study solid tumor (*carcinoma*) growth in the nonlinear regime using boundary-integral simulations. The tumor core is nonnecrotic and no inhibitor chemical species are present. A new formulation of the classical models [18,24,8,3] is developed and it is demonstrated that tumor evolution is described by a reduced set of two dimensionless parameters and is qualitatively unaffected by the number of spatial dimensions. One parameter describes the relative rate of mitosis to the relaxation mechanisms (cell mobility and cell-to-cell adhesion). The other describes the balance between apoptosis (programmed cell-death) and mitosis. Both parameters also include the effect of vascularization.

Our analysis and nonlinear simulations reveal that the two new dimensionless groups uniquely subdivide tumor growth into three regimes associated with increasing degrees of vascularization: low (diffusion dominated, e.g., *in vitro*), moderate and high vascularization, that correspond to the regimes observed *in vivo*. We demonstrate that critical conditions exist for which the tumor evolves to nontrivial dormant states or grows self-similarly (i.e., shape invariant) in the first two regimes. This leads to the possibility of shape control and of controlling the release of tumor angiogenic factors by restricting the tumor volume-to-surface-area ratio. Away from these critical conditions, evolution may be unstable leading to invasive fingering into the external tissues and to topological transitions such as tumor breakup and reconnection. Interestingly we find that for highly vascularized tumors, while they grow unbounded, their shape always stays compact and invasive fingering does not occur. This is in agreement with recent experimental observations [30] of *in vivo* tumor growth, and suggests that the invasive growth of highly-vascularized tumors is associated to vascular and elastic anisotropies, which are not included in the model studied here.

1. Introduction

Tumor growth is a fundamental scientific problem and has received considerable attention by the mathematics community (see for example the recent review papers [1,9,2]). Here we focus on a continuum-scale description and pose the problem in terms of conservation laws for the nutrient and tumor-cell concentrations, using a new formulation of an existing model [18,7,14]. This model describes evolution

V. Cristini, J. Lowengrub: School of Mathematics, and Department of Chemical Engineering and Materials Science, University of Minnesota, Minneapolis MN 55455.

Current address: Department of Biomedical Engineering, and Department of Mathematics, University of California at Irvine, Irvine CA 92697. e-mail: cristini@math.uci.edu; lowengrb@math.umn.edu.

Q. Nie: Department of Mathematics, University of California at Irvine, Irvine CA 92697. e-mail: qnie@math.uci.edu.

Key words or phrases: Tumor growth – Linear stability analysis – Self-similarity – Boundary-integral simulations

of avascular and vascularized tumors, but not the angiogenetic transition between the two.

The tumor is treated as an incompressible fluid and tissue elasticity is neglected. Cell-to-cell adhesive forces are modeled by a surface tension at the tumor-tissue interface. The growth of tumor mass is governed by a balance between cell mitosis and apoptosis (programmed cell-death). The rate of mitosis depends on the concentration of nutrient and inhibitor chemical species, that obey diffusion-reaction equations in the tumor volume. The bulk source of chemical species is the blood. The concentration of capillaries in the tumor is assumed to be uniform as are the concentrations of chemical species in the external tissues. In this paper we focus on the case of nonnecrotic tumors (i.e., Phase I tumors) [7] with no inhibitor chemical species. These conditions apply to small-sized tumors, or when the nutrient concentrations in the blood and in the external tissues are high. We anticipate that such a model should over-predict growth away from these conditions.

We present a new formulation of the mathematical model and we study tumor growth using boundary-integral simulations in the nonlinear regime to explore complex tumor morphologies. To our knowledge, these are the first fully nonlinear simulations of a continuum model of tumor growth, and represent a step towards the development of a computer simulator of cancer, as will be discussed in more detail in the Conclusions. We note that there has been recent work on cellular automata-based simulations of tumor growth (e.g. see [19] and the references therein). Our new formulation demonstrates that tumor evolution is described by a reduced set of two parameters that characterize families of solutions. The parameter G describes the relative rate of mitosis to the relaxation mechanisms (cell mobility and cell-to-cell adhesion). The parameter A describes the balance between apoptosis and mitosis. Both parameters also include the effect of vascularization. Our analysis reveals that tumor evolution is qualitatively unaffected by the number of spatial dimensions. Thus, here we focus our nonlinear simulations on 2D tumor geometries. Our study reveals that the two new dimensionless groups uniquely subdivide tumor growth into three regimes associated with increasing degrees of vascularization: low (diffusion dominated, e.g., *in vitro*), moderate and high vascularization, that correspond to the regimes observed in *in vivo* experiments. We demonstrate that critical conditions exist for which the tumor evolves to nontrivial dormant states or grows self-similarly (i.e., shape-invariant) in the first two regimes in the full nonlinear system. Explicit examples of these behaviors are given using nonlinear simulations. The existence of non-trivial dormant states was recently proved [13], but no examples of such states were given.

The self-similar behavior described here is analogous to that recently found in diffusional crystal growth [12], and leads to the possibility of shape control and of controlling the release of tumor angiogenic factors by restricting the tumor volume-to-surface-area ratio. This could restrict angiogenesis during growth. Away from these critical conditions, evolution may lead to invasive fingering into the external tissues and to topological transitions such as tumor breakup and reconnection. Interestingly we find that, in the high-vascularization regime, while the tumor grows unbounded the tumor shape always stays compact and invasive fingering does not occur. This is in agreement with recent experimental observations [30] of *in vivo*

tumor growth in a isotropic sponge-like matrix, and suggests that the invasive growth of highly-vascularized tumors is associated to vascular and elastic anisotropies, which are not included in the model investigated here.

In Sect. 2, our new formulation for nonnecrotic tumors is presented, analytic results for radially symmetric tumors are revisited and the regimes of growth are identified. Our linear analysis in two and three dimensions is presented in Sect. 2.3. In Sect. 2.3.1, self-similar tumor evolution is investigated. Nonlinear simulations are presented in Sect. 4. Our conclusions and directions for future work are in Sect. 5.

2. Problem formulation and linear analysis

2.1. New formulation

The classical mathematical model [18,24,8,3] describing the evolution of nonnecrotic tumors in the absence of inhibitor chemical species is summarized in Appendix A. It is shown that the model system considered has only one intrinsic length scale: the diffusional length L_D, and has three intrinsic time scales corresponding to the relaxation rate λ_R (associated to L_D, cell mobility and cell-to-cell adhesion), the characteristic mitosis rate λ_M and the apoptosis rate λ_A. By using algebraic manipulations, it can be shown that the dimensional problem stated in Appendix A can be reformulated in terms of two nondimensional decoupled problems:

$$\begin{aligned} \nabla^2 \Gamma - \Gamma &= 0, \\ (\Gamma)_\Sigma &= 1; \end{aligned} \tag{1}$$

and

$$\begin{aligned} \nabla^2 p &= 0, \\ (p)_\Sigma &= \kappa - A\, G\, \frac{(\mathbf{x}\cdot\mathbf{x})_\Sigma}{2d}, \end{aligned} \tag{2}$$

in a d–dimensional tumor. Here, space and time have been normalized with the intrinsic scales L_D and λ_R^{-1}, the interface Σ separates the tumor volume from the external tissue, and the variables Γ and p represent a modified nutrient concentration and a modified pressure (see Appendix A for their definitions). The tumor surface Σ (of local total curvature κ) is evolved using the normal velocity

$$V = -\mathbf{n}\cdot(\nabla p)_\Sigma + G\,\mathbf{n}\cdot(\nabla\Gamma)_\Sigma - A\,G\,\frac{\mathbf{n}\cdot(\mathbf{x})_\Sigma}{d}, \tag{3}$$

where $\mathbf{n}$ is the outward normal to Σ and $\mathbf{x}$ is position in space. The instantaneous problem stated above has only two dimensionless parameters:

$$\begin{aligned} G &= \frac{\lambda_M}{\lambda_R}\,(1-B)\,, \\ A &= \frac{\lambda_A/\lambda_M - B}{1-B}. \end{aligned} \tag{4}$$

The former describes the relative strength of cell mitosis to the relaxation mechanisms, and the latter describes the relative strength of cell apoptosis and mitosis. The effect of vascularization is in the parameter B defined in Appendix A. Note that in the context of steady solutions, the parameter A is related to the parameter Λ introduced in [7] by $A = 3\Lambda$.

We define the rescaled rate of change of tumor volume $H = \int_\Omega \mathrm{d}\mathbf{x}^d$ as the mass flux $J = \frac{\mathrm{d}}{\mathrm{d}t} H = \int_\Sigma V \mathrm{d}\mathbf{x}^{d-1}$. By using (1a)–(2a) we obtain from (3):

$$J = -G \int_\Omega \Gamma \, \mathrm{d}\mathbf{x}^d - A\, G\, H. \tag{5}$$

2.2. Regimes of growth

In order to identify the regimes of growth, we consider evolution of a tumor that remains radially symmetric. The interface Σ is an infinite cylinder for $d = 2$ or a sphere for $d = 3$, with radius $R(t)$. All the variables have only r–dependence, where r is the polar coordinate. Equations (1)–(2) have the nonsingular solutions

$$\Gamma(r,t) = \begin{cases} \dfrac{I_0(r)}{I_0(R)}, & d = 2, \\ \left(\dfrac{\sinh(R)}{R}\right)^{-1} \dfrac{\sinh(r)}{r}, & d = 3, \end{cases} \tag{6}$$

and $p(r,t) = (d-1)R^{-1} - AGR^2/(2d)$. Note that $p(r,t) \equiv p(R,t)$, i.e., p is uniform across the tumor volume.

From equation (3) the evolution equation for the tumor radius R is:

$$\frac{\mathrm{d}R}{\mathrm{d}t} = V = -AG\,\frac{R}{d} + G \begin{cases} \dfrac{I_1(R)}{I_0(R)}, & d = 2. \\ \dfrac{1}{\tanh(R)} - \dfrac{1}{R}, & d = 3. \end{cases} \tag{7}$$

Note that for a radially symmetric tumor, $|G|$ rescales time and it can be shown that $V = G - AGR$ for $d = 1$, where R is defined for $d = 1$ as the instantaneous position of the interface, with $R(0) = 0$. In all dimensions, unbounded growth ($R \to \infty$) occurs if and only if $AG \leq 0$. The growth velocity is plotted for $d = 2$ in figure 1. Note that, for $d = 3$, the results are qualitatively similar and were reported in figure 9 in [7], although in the framework of the original formulation the growth regimes had not been identified. The figure is included here to identify the growth regimes. For given A, evolution from initial condition $R(0) = R_0$ occurs along the corresponding curve. Three regimes are identified, and the behavior is qualitatively unaffected by the number of spatial dimensions d.

1. *Low vascularization*: $G \geq 0$ and $A > 0$ (i.e., $B < \lambda_A/\lambda_M$). Note that the special case of avascular growth ($B = 0$) belongs to this regime. Evolution is monotonic and always leads to a stationary state R_∞, that corresponds to the intersection of the curves in figure 1 with the dotted line $V = 0$. This behavior is in agreement with the experimental observations of *in vitro* diffusional

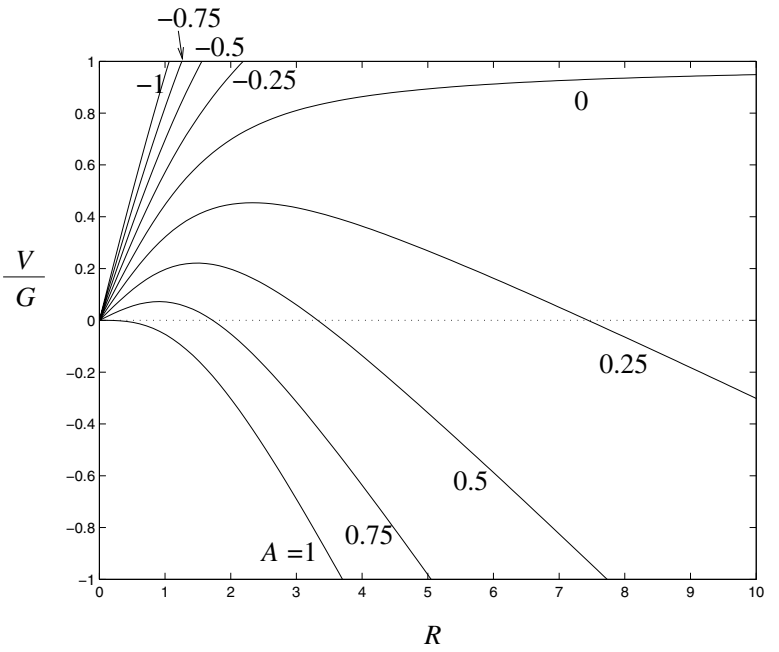

Fig. 1. Rescaled rate of growth $G^{-1}V$ from equation (7) as a function of rescaled tumor radius R for radially symmetric tumor growth and $d = 2$; A labelled.

growth [17] of multicell avascular spheroids to a dormant steady state [26,35]. In the experiments, however, the tumors always develop a necrotic core which further stabilizes their growth [6].

2. *Moderate vascularization*: $G \geq 0$ and $A \leq 0$ (i.e., $1 > B \geq \lambda_A/\lambda_M$). Unbounded growth occurs from any initial radius $R_0 > 0$. The growth tends to exponential for $A < 0$ with velocity $V \to -AGR/d$ as $R \to \infty$, and to linear for $A = 0$ with velocity $V \to G$ as $R \to \infty$.
3. *High vascularization*: $G < 0$ (i.e., $B > 1$). Growth ($V > 0$) may occur, depending on the initial radius, for $A > 0$, and is always unbounded; for $A < 0$ (for which cell apoptosis is dominant: $\lambda_A/\lambda_M > B$), the evolution is always to the only stationary solution $R_\infty = 0$. This stationary solution may also be achieved for $A > 0$.

The stationary radius R_∞ is independent of G, and is solution of $V = 0$ with V from equation (7). The stationary radius has limiting behaviors

$$\begin{aligned} &R_\infty \to d\, A^{-1}, \quad A \to 0, \\ &R_\infty \to d^{\frac{1}{2}}(d+2)^{\frac{1}{2}}\,(1-A)^{\frac{1}{2}}, \quad A \to 1, \end{aligned} \tag{8}$$

where R_∞ vanishes. Note that the limit $A \to 1$ corresponds to $\lambda_A \to \lambda_M$. For $d = 1$ the stationary radius is $R_\infty = A^{-1}$ identically.

The pressure P_C (see Appendix A) at the center of the tumor ($r \equiv 0$) is obtained from equation (54b):

$$\frac{P_C}{(\gamma/L_D)} = (d-1)/R + G - A\,G\,R^2/(2d) - G \begin{cases} 1/I_0(R), & d=2, \\ R/\sinh(R), & d=3, \end{cases} \tag{9}$$

which has the asymptotic behavior $P_C\ (\gamma/L_D)^{-1} \to -AGR^2/(2d)$ as $R \to \infty$, indicating that if the tumor grows unbounded ($AG \leq 0$) the pressure at the center also does (unless $A = 0$). This is a direct consequence of the absence of a necrotic core in this model. In a real system, the increasing pressure may itself contribute to necrosis [27–29]. It is known (see, for example, [9]) that tumor cells continuously replace the loss of cell volume in a tumor's core because of necrosis, thus maintaining pressure finite. For $d = 1$ we define P_C as the limit of P as $R \to -\infty$, and it can be shown that $P_C\ (\gamma/L_D)^{-1} = G$.

2.3. Linear analysis

We consider a perturbation of the spherical tumor interface Σ:

$$R(t) + \delta(t) \begin{cases} \mathrm{e}^{\mathrm{i}l\theta}, & d=2, \\ Y_{l,m}(\theta,\phi), & d=3, \end{cases} \tag{10}$$

where δ is the dimensionless perturbation size and $Y_{l,m}$ is a spherical harmonic, where l and θ are polar wavenumber and angle, and m and ϕ azimuthal wavenumber and angle.

By solving the system of equations (1)–(3) in the presence of a perturbed interface we obtain the evolution equation (7) for the unperturbed radius R and the evolution equation for the perturbation size δ:

$$\delta^{-1}\,\frac{\mathrm{d}\delta}{\mathrm{d}t} = \begin{cases} l\left(\dfrac{J}{2\pi R^2} + A\,G\right) - \dfrac{A\,G}{2} \\ \quad +G - \left(\dfrac{J}{2\pi R} + A\,G\,\dfrac{R}{2}\right)\dfrac{I_{l-1}(R)}{I_l(R)} - \dfrac{l\left(l^2-1\right)}{R^3} - \dfrac{G\,I_1(R)}{R\,I_0(R)}, & d=2, \\ \\ G - A\,G - \dfrac{(l+2)\,J}{4\pi R^3} - \dfrac{l(l-1)(l+2)}{R^3}, & d=3, \end{cases} \tag{11}$$

where the dimensionless flux

$$J = 2\pi\,(d-1)\,R^{d-1}\,V + O\,(\delta/R)^2\,, \tag{12}$$

with V given by (7). Note that the linear evolution of the perturbation is independent of the azimuthal wavenumber m and there is a critical mode l_c such that perturbations grow for $l < l_c$ and decay for $l > l_c$. The critical mode depends on the parameters A, G and the evolving radius R. This agrees with the linear

analyses presented in [18,7,5] for the special case where the unperturbed configuration is stationary (i.e. R constant). Also, for $d = 1$ it can be shown that $\delta^{-1}\frac{\mathrm{d}}{\mathrm{d}t}\delta = -l^3 - G\left(\left(l^2+1\right)^{\frac{1}{2}} - 1\right) + AG\,(lR-1)$.

During unbounded growth, $AG \leq 0$ and perturbations decay to zero for $d = 1, 2$ since $\delta^{-1}\frac{\mathrm{d}}{\mathrm{d}t}\delta \to lAGR < 0$ for $d = 1$ and $\delta^{-1}\frac{\mathrm{d}}{\mathrm{d}t}\delta \to (l-1)AG/2 < 0$ for $d = 2$, as $R \to \infty$. For $d = 3$, $\delta^{-1}\frac{\mathrm{d}}{\mathrm{d}t}\delta \to 0$, as $R \to \infty$, for $A = -3(l-1)^{-1}$, and perturbations grow (decay) for A larger (smaller) than this value.

2.3.1. Shape evolution and conditions for self-similarity

Here, we characterize the evolution of the perturbed shape using the shape factor δ/R (following Ref. [12]), governed by

$$(\delta/R)^{-1}\frac{\mathrm{d}}{\mathrm{d}t}(\delta/R) = \delta^{-1}\frac{\mathrm{d}\delta}{\mathrm{d}t} - \frac{J}{2\pi\,(d-1)\,R^d}. \tag{13}$$

Thus, when

$$\frac{\mathrm{d}}{\mathrm{d}t}(\delta/R) = 0$$

the tumor shape does not change in time and the evolution is linearly self-similar (sometimes also referred to as neutral stability). This condition divides regimes of stable ($\delta/R \to 0$) and unstable ($|\delta/R| \to \infty$) growth.

Let us investigate conditions for which the tumor grows unbounded but self-similarly, thus maintaining its shape. This should have implications for angiogenesis, or tumor vascularization. It is known that angiogenesis occurs as tumor angiogenetic factors are released within the tumor, and migrate to nearby vessels triggering the chemotaxis of endothelial cells and thus the formation of a network of blood vessels that finally penetrate the tumor providing unlimited supply of nutrients and thus typically resulting in malignancy. Assuming the flux of angiogenic factors to be proportional to the tumor/tissue interface area, and the rate of production of angiogenic factors to be proportional to the tumor volume, we conclude that self-similar evolution divides tumor growth in two categories: one (stable growth) characterized by a decrease of the area-to-volume ratio during growth thus hampering or preventing angiogenesis, the other (unstable growth) characterized by an increase of the area-to-volume ratio and thus favoring angiogenesis.

In Sect. 4.3 the possibility of shape control, by "tuning" the parameter conditions to impose self-similar growth, will be investigated in detail. Here we investigate the possibility of self-similar evolution using constant parameters in the limit as the effective tumor radius $R \to \infty$.

The asymptotic behavior of the flux J as $R \to \infty$ is, from (7) and (12), $J \to -2\pi\,(d-1)\,A\,G\,R^d/d$. Note that if the tumor grows unbounded then $A\,G \leq 0$. For $d = 3$, it is easily shown from (11) and (13) that $(\delta/R)^{-1}\frac{\mathrm{d}}{\mathrm{d}t}(\delta/R) \to G\,(1 + Al/3)$ as $R \to \infty$ and thus there exists a critical

$$A_l = -3l^{-1}, \tag{14}$$

such that for $A = A_l$ we obtain

$$\frac{\mathrm{d}}{\mathrm{d}t}\,(\delta/R) \to 0 \quad \text{as} \quad \mathrm{R} \to \infty,$$

and the growing tumor tends to self-similar (shape invariant) evolution. Under constant parameter conditions, unbounded growth that tends to self-similar is possible only in the moderate-vascularization regime characterized by $G > 0$ and $A < 0$. For $A > A_l$ the perturbation grows unbounded with respect to the growing unperturbed radius; for $A < A_l$ it decays to zero. In the high-vascularization regime ($G < 0$), unbounded growth ($A > 0$) is always stable.

For $d = 2$ the perturbation always decays to zero thus leading to stable unbounded growth, since $(\delta/R)^{-1}\,\frac{\mathrm{d}}{\mathrm{d}t}\,(\delta/R) \to AGl/2$ as $R \to \infty$ for $A \neq 0$. Thus in particular self-similar long-time behavior during growth with constant parameters is a peculiarity of three dimensions only. Moreover, in two dimensions unstable (bounded) growth is possible only in the low-vascularization regime. In Sect. 4.3 and in Appendix B we demonstrate that unstable and self-similar unbounded growth are possible, both for $d = 2$ and $d = 3$, by varying the dimensionless parameters A and G in time. Interestingly, these results reveal that growth for $d = 2$ and 3 has the same qualitative features.

3. Numerical method

3.1. Boundary integral formulation

In two dimensions, the interface $\Sigma \equiv \partial\Omega(t)$ is represented by a planar curve, with arclength s. From potential theory, Γ can be expressed using a double-layer potential ν:

$$\Gamma\,(\mathbf{x}) = -(2\pi)^{-1} \int_{\Sigma} \nu'\,\mathbf{n}' \cdot \nabla K_0\left(\left|\mathbf{x}' - \mathbf{x}\right|\right)\,\mathrm{d}s', \tag{15}$$

where $\mathbf{n}$ is the outward normal of Σ, the prime indicates quantities evaluated at the position s' on the interface, and the Green's function is $-(2\pi)^{-1}K_0$, where K_0 is the modified Bessel function [10]. Let Σ be parameterized counterclockwise by $\mathbf{x}(\alpha) \equiv (x(\alpha), y(\alpha))$ with the arbitrary parameter $\alpha \in [0, 2\pi]$ such that $\mathrm{d}s = \left(x_\alpha^2 + y_\alpha^2\right)^{\frac{1}{2}}\,\mathrm{d}\alpha$. Taking the limit of equation (15) for $\mathbf{x} \to \mathbf{x}\,(s) \in \Sigma$, the boundary condition (1b) becomes a second-kind Fredholm integral equation on the boundary Σ:

$$\frac{\nu(\alpha)}{2} + \int_0^{2\pi} \nu(\alpha')\,\mathcal{K}\left(\alpha, \alpha'\right)\,\mathrm{d}\alpha' = 1 \tag{16}$$

where

$$\mathcal{K}\left(\alpha, \alpha'\right) = \left((x(\alpha') - x(\alpha))\,y_{\alpha'} - (y(\alpha') - y(\alpha))\,x_{\alpha'}\right)\frac{K_1(r)}{2\pi r} \tag{17}$$

with $r = \left((x(\alpha') - x(\alpha))^2 + (y(\alpha') - y(\alpha))^2\right)^{\frac{1}{2}}$, and a subscript indicates differentiation. In deriving equation (16), we have used

$$\frac{\mathrm{d}}{\mathrm{d}r}K_0(r) = -K_1(r). \tag{18}$$

The kernel $\mathcal{K}$ has a logarithmic singularity at $\alpha = \alpha'$:

$$\mathcal{K}\left(\alpha, \alpha'\right) = L_1\left(\alpha, \alpha'\right) \ln\left(4\sin^2\frac{\alpha - \alpha'}{2}\right) + L_2\left(\alpha, \alpha'\right), \tag{19}$$

where L_1 and L_2 are analytic and periodic [23, 11]:

$$L_1\left(\alpha, \alpha'\right) = \left(\left(x(\alpha') - x(\alpha)\right)\, y_{\alpha'} - \left(y(\alpha') - y(\alpha)\right)\, x_{\alpha'}\right) \frac{I_1(r)}{4\pi r}, \tag{20}$$

$$L_2\left(\alpha, \alpha'\right) = \mathcal{K}\left(\alpha, \alpha'\right) - L_1\left(\alpha, \alpha'\right) \ln\left(4\sin^2\frac{\alpha - \alpha'}{2}\right), \tag{21}$$

and $I_1(r)$ is the modified Bessel function. Note that

$$L_2(\alpha, \alpha) = \frac{1}{4\pi}\frac{y_{\alpha\alpha}x_\alpha - x_{\alpha\alpha}y_\alpha}{x_\alpha^2 + y_\alpha^2}. \tag{22}$$

For the computation of p, a dipole-layer representation [25] is used with the dipole-layer potential η. We recast equation (2b) in terms of a second-kind Fredholm integral equation on the boundary Σ [15, 21]:

$$-\frac{\eta(\alpha)}{2} + \frac{1}{2\pi}\int_0^{2\pi} \eta(\alpha') \frac{(x(\alpha) - x(\alpha'))y_{\alpha'} - (y(\alpha) - y(\alpha'))x_{\alpha'}}{(x(\alpha) - x(\alpha'))^2 + (y(\alpha) - y(\alpha'))^2} \mathrm{d}\alpha' = \kappa - AG\,\frac{x(\alpha)^2 + y(\alpha)^2}{4}. \tag{23}$$

The normal velocity V in equation (3) requires the evaluation of the normal derivatives $\mathbf{n}\cdot\nabla\Gamma$ and $\mathbf{n}\cdot\nabla p$. We first discuss the former. The normal derivative of the double layer potential can be written in terms of a single layer potential S [22, 10]:

$$\mathbf{n}\cdot\nabla\Gamma\,(s) = \frac{\mathrm{d}}{\mathrm{d}s} S\left(\nu_s\right) - \mathbf{n}\,(s)\cdot S\left(\mathbf{n}\nu\right), \tag{24}$$

where

$$S\left(\mathbf{P}\right) \equiv -(2\pi)^{-1}\int_\Sigma \mathbf{P}\left(s'\right) K_0\left(\left|\mathbf{x}\,(s) - \mathbf{x}\left(s'\right)\right|\right) \mathrm{d}s', \tag{25}$$

for any vector (or scalar) $\mathbf{P}$. In (25), the function K_0 has a logarithmic singularity at $s = s'$, and a decomposition similar to equation (19) can be performed.

The normal derivative of p is computed using the Dirichlet-Neumann map [25, 15, 21]:

$$\mathbf{n}\cdot\nabla p\,(\alpha) = \frac{1}{2\pi}\int_0^{2\pi} \eta_{\alpha'} \frac{(x(\alpha) - x(\alpha'))\, y_{\alpha'} + (y(\alpha) - y(\alpha'))\, x_{\alpha'}}{(x(\alpha) - x(\alpha'))^2 + (y(\alpha) - y(\alpha'))^2} \mathrm{d}\alpha', \tag{26}$$

where the principal value of the integral is taken.

3.2. Surface representation and quadrature

We discretize the planar curve describing the surface Σ using N marker points, with parametrization $\alpha_j = jh$, $h = 2\pi/N$, N is a power of 2. For an analytic and periodic function L_1, the following quadrature formula is spectrally accurate [16]:

$$\int_0^{2\pi} L_1\left(\alpha_i, \alpha'\right) \ln\left(4\sin^2\frac{\alpha_i - \alpha'}{2}\right) \mathrm{d}\alpha' \approx \sum_{j=0}^{2n-1} w_{|j-i|} L_1(\alpha_i, \alpha_j) \tag{27}$$

for $\alpha_i = \pi i/n$, $i = 0, ..., 2n-1$, $n = N/2$, where

$$w_j = -\frac{2\pi}{n}\sum_{m=1}^{n-1}\frac{1}{m}\cos\frac{mj\pi}{n} - \frac{(-1)^j\pi}{n^2}, \qquad j = 0, ..., 2n-1. \tag{28}$$

We use the standard composite trapezoidal rule for the integral involving the kernel L_2, yielding spectral accuracy.

To compute $S(\mathbf{P})$ we employ the same computational strategy for (24) as used for the kernel L_1. The derivatives $\mathrm{d}/\mathrm{d}s$ in (24) are approximated using Fast-Fourier-Transform spectral derivatives. As a result, $\mathbf{n}\cdot\nabla\Gamma$ is discretized with spectral accuracy.

In equations (23) and (26), the integrals are calculated using the alternating-point trapezoidal quadrature also yielding spectral accuracy [34].

Using the collocation method with the quadrature rules described above, we reduce the boundary integral equations (16) and (23) to a dense linear system, which is then solved using an iterative solver GMRES [31]. Following [32,21], a 15th order Fourier filter is used to reduce aliasing errors. Moreover, during a simulation, marker points are added by multiples of 2 (using trigonometric interpolation) when the amplitude of the Nyquist frequency ($N/2$) exceeded the tolerance for solving the integral equation.

3.3. Surface evolution

To evolve the tumor surface $\Sigma(t)$, we follow [32,21] and use the tangent-angle/area formulation in a scaled arclength frame defined by

$$\mathrm{d}s = \frac{L}{2\pi}\mathrm{d}\alpha, \tag{29}$$

where $L(t)$ is the length of the tumor surface. This implies that the collocation points are equally spaced in arclength. Accordingly, we evolve the tumor surface using the tangential velocity

$$T(\alpha) = \frac{\alpha}{2\pi}\int_0^{2\pi}\theta_{\alpha'}V'\mathrm{d}\alpha' - \int_0^{\alpha}\theta_{\alpha'}V'\mathrm{d}\alpha', \tag{30}$$

where $\theta(\alpha)$ is the angle between the tangent to the tumor surface and the x-axis:

$$x_\alpha = \frac{L}{2\pi}\cos\theta \qquad y_\alpha = \frac{L}{2\pi}\sin\theta, \tag{31}$$

and V is the normal velocity. The length $L(t)$ and the area $H(t)$ of the tumor are related by

$$H(t) = \frac{L^2}{8\pi^2} \int_0^{2\pi} \int_0^{\alpha} \sin\left(\theta - \theta'\right) \mathrm{d}\alpha' \, \mathrm{d}\alpha. \tag{32}$$

The evolution of the tumor surface is reposed in terms of $\theta(\alpha, t)$, $H(t)$, and the centroid (x_c, y_c). The time-derivatives are

$$\dot{\theta}(\alpha, t) = \frac{2\pi}{L} \left(V_\alpha + T\ \theta_\alpha\right), \qquad \dot{H}(t) = \int_\Sigma V \mathrm{d}s, \tag{33}$$

$$\dot{x}_c(t) = \frac{1}{H} \left(\int_\Sigma x\ V \mathrm{d}s - x_c \dot{H} \right), \qquad \dot{y}_c(t) = \frac{1}{H} \left(\int_\Sigma y\ V \mathrm{d}s - y_c \dot{H} \right). \tag{34}$$

It can be shown that from equations (1–3), for our problem $\dot{x}_c = \dot{y}_c = 0$. After a time step, the point positions on the surface are reconstructed using (31)–(32), with integration constant determined from (34).

Following [32], we can show that, at small spatial scales,

$$V \sim \left(\frac{2\pi}{L}\right)^2 \mathcal{H}\left(\theta_{\alpha\alpha}\right) \tag{35}$$

where $\mathcal{H}(\xi) = (4\pi)^{-1} \int_0^{2\pi} \xi' \cot((\alpha - \alpha')/2) \mathrm{d}\alpha'$ is the Hilbert transformation for any scalar ξ. This demonstrates that an explicit time-stepping scheme has the high-order constraint $\Delta t \leq (hL/2\pi)^3$, where Δt and h are the temporal and spatial grid sizes. In [32] and later in [21], time stepping methods based on an integration factor and Crank-Nicholson discretizations have been developed to reduce the stability constraint. In this paper, we use a Crank-Nicholson discretization and a $O(\Delta t)^2$ method based on an integration factor [32].

4. Results

4.1. Unstable growth

Here, we investigate unstable evolution in the low-vascularization (diffusion dominated) regime, characterized by $G, A > 0$, for $d = 2$ using nonlinear boundary-integral simulations. The linear analysis in Sect. 2.3.1 demonstrates that evolution in the other regimes is stable for $d = 2$. In Figure 2, the evolution of the tumor surface from a nonlinear boundary-integral simulation with $N = 1024$ and $\Delta t = 10^{-3}$ (solid curve) is compared to the result of the linear analysis (dotted). In this case $A = 0.5$, $G = 20$, and the initial shape of the tumor is

$$(x(\alpha), y(\alpha)) = (2 + 0.1 \cos 2\alpha)\ (\cos\alpha, \sin\alpha)\,. \tag{36}$$

According to linear theory (formula (7) and figure 1), the tumor grows. The radially symmetric equilibrium radius $R_\infty \approx 3.32$. Mode $l = 2$ is linearly stable initially, and becomes unstable at $R \approx 2.29$. The linear and nonlinear results in figure 2 are indistinguishable up to $t = 1$, and gradually deviate thereafter. Correspondingly, a shape instability develops and forms a neck. At $t \approx 1.9$, the linear solution collapses

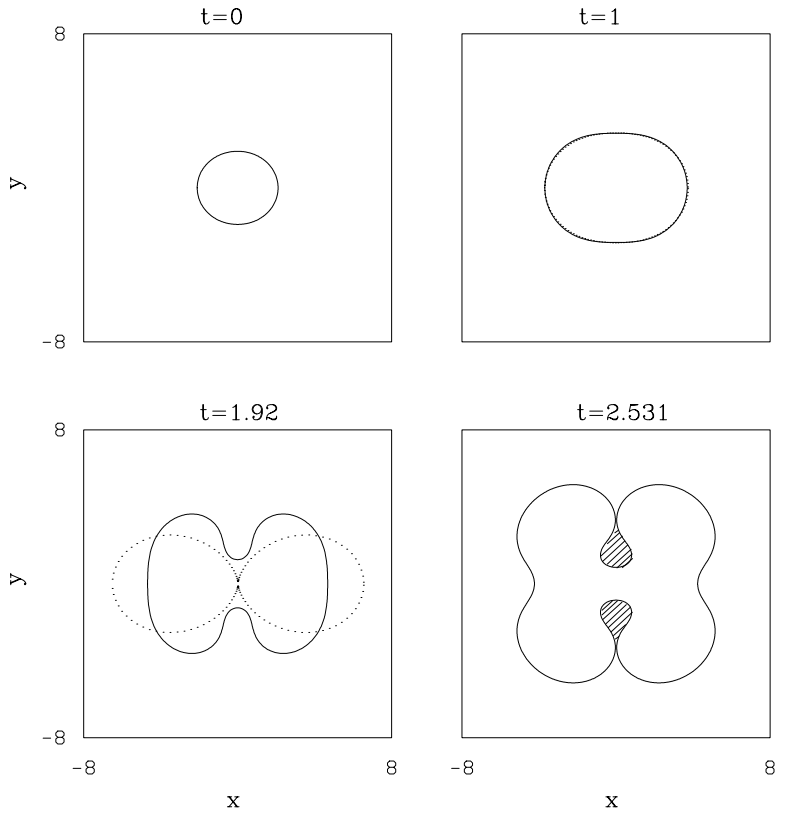

Fig. 2. Evolution of the tumor surface in the low-vascularization regime, for $d = 2$, $A = 0.5$, $G = 20$, and initial tumor surface as in equation (36). Dotted lines: solution from linear analysis; solid: solution from a nonlinear calculation with time step $\Delta t = 10^{-3}$ and a number of marker points $N = 1024$, reset, after time $t = 2.51$, to $\Delta t = 10^{-4}$ and $N = 2048$.

suggesting pinch-off; the nonlinear solution is stabilized by the cell-to-cell adhesive forces (surface tension) that resist the development of high negative curvatures in the neck. This is not captured by the linear analysis. Instead of pinching off, as is predicted linear evolution, the nonlinear tumor continues to grow and develops large bulbs that eventually reconnect thus trapping healthy tissue (shaded regions in the last frame in Figure 2) within the tumor. The frame at $t = 2.531$ describes the onset of reconnection of the bulbs. We expect that reconnection would be affected by diffusion of nutrient outside the tumor, which is not included in the model used here. However, the predictions of the development of shape instabilities and of the capture of healthy tissue during growth are in agreement with experimental observations [33].

The accuracy of our nonlinear calculations is established by a resolution study of the simulation shown in Figure 2. First, the spatial error is investigated by varying the number N of collocation points representing the tumor surface. In Figure 3, the maximal differences in the tumor surface between a simulation with $N = 1024$ and

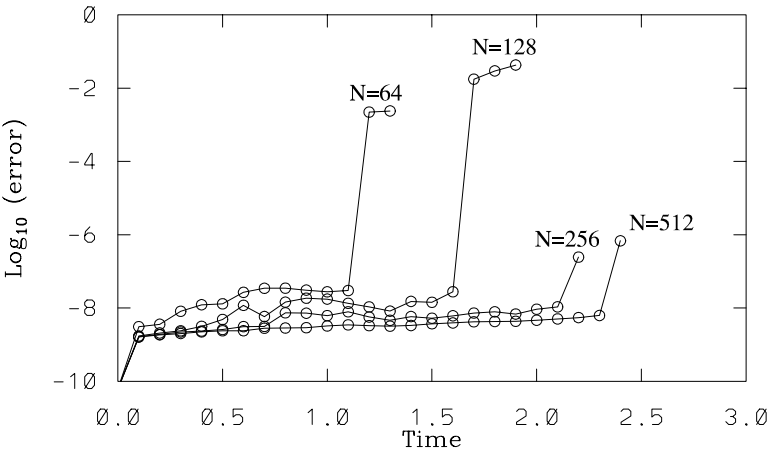

Fig. 3. Spatial resolution study for the case in figure 2: maximal differences between the solution calculated using $N = 1024$ and other smaller N.

others with smaller N are plotted as functions of time. In all cases the time step is $\Delta t = 10^{-3}$. The tolerance for solving the integral equations for Γ and p is 10^{-10}. At early times, the error is dominated by the tolerance in solving the equations; thus, the error decreases only slightly, from 10^{-8} to 10^{-9}, as N increases. This is consistent with the high-order accuracy of our discretization. The calculations for smaller N stop at much earlier times than those for larger N due to the failure in solving the integral equations with the given tolerance. Clearly, the solution computed using $N = 512$ is accurate to 10^{-9}, close to the tolerance 10^{-10}, until the tumor surface is about to pinch ($t \approx 2.5$).

The errors introduced by the temporal discretization are investigated in Figure 4. As for the spatial resolution study, the maximal differences in the tumor surface between the calculation using $\Delta t = 10^{-3}$ and others using larger $\triangle t$ are plotted as functions of time. In all cases $N = 256$. Since the temporal scheme is second-order accurate, an improvement in accuracy of a factor of 4 is obtained whenever Δt is halved demonstrating convergence.

Next, we demonstrate that the capture of healthy tissue due to nonlinear tumor reconnection is robust. Consider the evolution of an asymmetric, multimodal initial tumor surface:

$$(x(\alpha),\, y(\alpha)) = (2 + 0.24\cos 2\alpha + 0.2\sin 2\alpha + 0.12\cos 3\alpha + 0.1\sin 3\alpha + 0.08\cos 5\alpha + 0.14\sin 6\alpha)\,(\cos\alpha, \sin\alpha)\,, \quad (37)$$

for the same values of $G = 20$ and $A = 0.5$ used in figure 2. At $t = 0$ all modes are linearly stable, as can be demonstrated from formula (11). At early times of the evolution depicted in figure 5, modes $l = 2$ to 6 are first damped, but then become successively unstable as the tumor grows. As in Figure 2, a neck develops on the tumor surface followed by the formation and asymmetric reconnection of bulbs ($t = 1.85$). An extension of our algorithm to describe evolution though topological transitions, such as reconnection, is in progress.

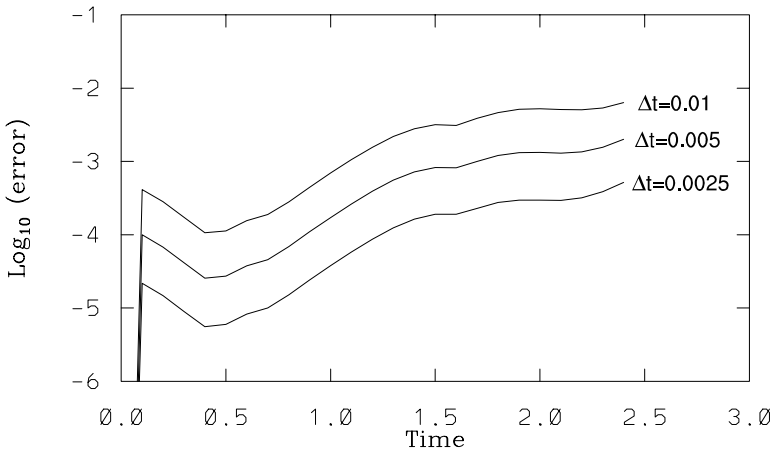

Fig. 4. Temporal resolution study: maximal differences between the solution calculated using $\Delta t = 10^{-3}$ and other larger Δt.

To conclude, we have found that during unstable evolution the linear and nonlinear solutions deviate from one another with the nonlinear solution being stabilized against pinchoff and leading instead to tumor reconnection and encapsulation of healthy tissue at later times as observed experimentally [33]. Finally, we find that reconnection occurs even when the amount of apoptosis is increased as is demonstrated in figure 6 where $A = 0.6$ and $G = 20$. The initial data for this simulation is asymmetric which thus leads to asymmetric reconnection. As before, the dashed curve is the solution from the linear analysis which now is a superposition of modes.

4.2. Nontrivial stationary states

In this section we present examples of nontrivial nonlinear stationary states in the low-vascularization regime. That such states exist was recently proved [13], and is predicted by linear theory. To see this, let us consider the linear evolution of a perturbation of a stationary radius R_∞. The stationary radius is solution of (7) with $V = 0$ (see also the related text), and is a function of $0 < A < 1$. Thus, the flux $J = 0$ and equation (11) gives that there exists a critical

$$G_l = \begin{cases} R_\infty^{-3} \dfrac{2l\left(l^2-1\right)}{2 + A\left(2(l-1) - R_\infty\, I_{l-1}(R_\infty)/I_l(R_\infty)\right)}, & d = 2 \\ \\ R_\infty^{-3} \dfrac{l\,(l-1)\,(l+2)}{1-A}, & d = 3 \end{cases} \tag{38}$$

such that for $G = G_l$ the perturbation also remains stationary. It can be shown that, for both $d = 2$ and 3, $G_l > 0$ and a perturbed stationary shape always exists. The perturbation δ/R_∞ grows unbounded for $G > G_l$ and decays to zero for $G < G_l$. At large radii R_∞, $G_l \to 0$, thus in this limit perturbations of stationary states always grow unbounded. For $d = 1$, we obtain $G_l = l^3(1 - A + l - (1 + l^2)^{\frac{1}{2}})^{-1}$,

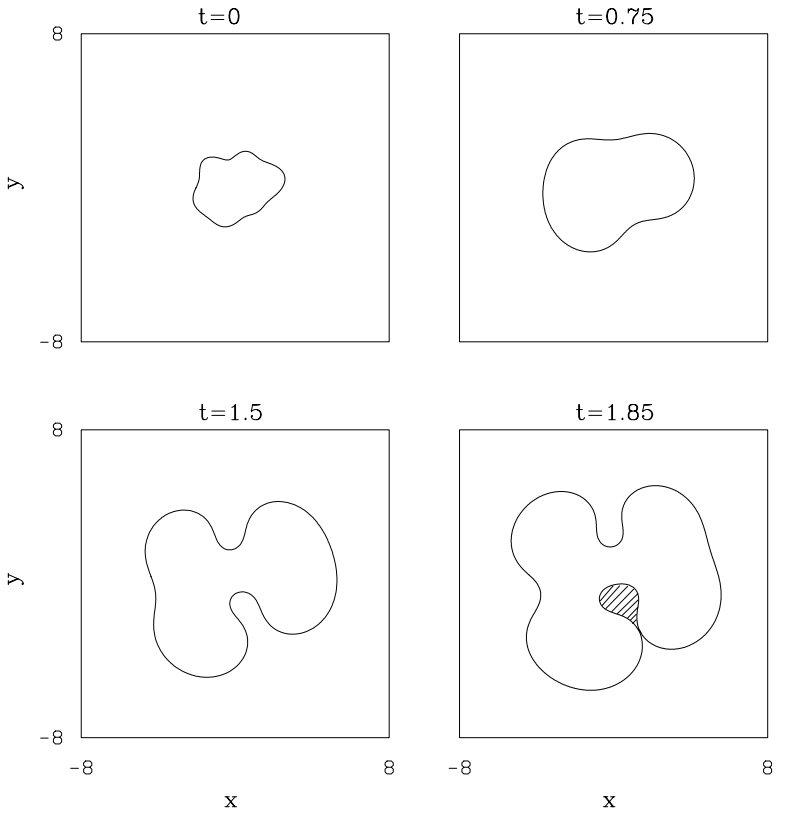

Fig. 5. Evolution in the low-vascularization regime from a boundary-integral simulation with $d = 2$, $G = 20$ and $A = 0.5$, and initial condition as in formula (37). The time step for the calculation is $\Delta t = 2 \times 10^{-4}$. The number of marker points $N = 512$ initially, and is gradually increased to 2048 by the end of the simulation ($t = 1.85$) as required by the highly deformed tumor surface.

which indicates that a nontrivial stationary solution may not exist, since G_l can be negative.

Let us next consider the nonlinear evolution for $d = 2$ of a mode l perturbation predicted by the linear theory to be stationary. The value of G is equal to G_l, with $R = R_\infty$, given in Eq. (38). Although the perturbations are linearly stationary, there is evolution due to nonlinearity. In figure 7 (top), the nonlinear evolution of several linearly stationary shapes in the low-vascularization regime is shown through their nonlinear perturbation size

$$\delta/R_0 = \max_j \left(|\mathbf{x_j}/R_0|^2 - 1 \right)^{1/2} \qquad j = 1, N,$$

where the maximum is taken over all the computational nodes of the interface. The corresponding evolution of the tumor cross-sectional area in the x-y plane is shown in figure 7 (bottom). The linear steady shape corresponds to $l = 4$, $A = 0.304$,

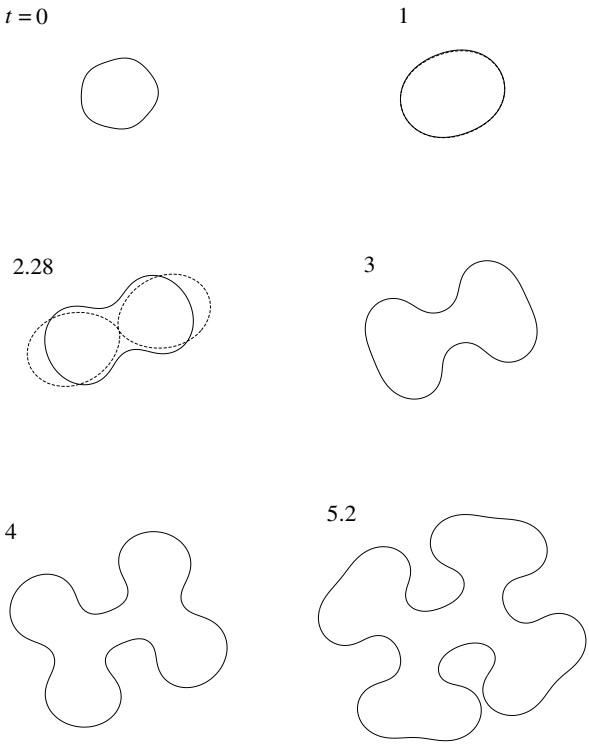

Fig. 6. Solid: nonlinear boundary-integral simulation of unstable growth of perturbation in the low-vascularization regime; $d = 2$, $G = 20$, $A = 0.6$, initial and stationary radii $R_0 = 2$ and $R_\infty = 2.5771$. Time is labeled. Dashed: linear result for same conditions.

$G = G_4 = 1.073$. Initially, $R_0 = 6$, and several initial perturbations are considered: $\delta_0/R_0 = 0.01, 0.05, 0.1, 0.2$. In addition, for each δ_0/R_0, several values of G are considered. In figure 7, the solid curves correspond to the choice $G = G_4$, the dotted curves to a value of $G \ll G_4$ and the dashed curves to a value of $G \approx G_4^{\mathrm{NL}} < G_4$, where G_4^{NL} represents a nonlinear critical value, that depends on the size of the perturbation, for which the numerical results predict evolution to a nontrivial nonlinear stationary state: δ/R becomes constant and non-zero. Here, we find only a numerical approximation to G_4^{NL}. For $G > G_4^{\mathrm{NL}}$ perturbations are nonlinearly unstable; for $G < G_4^{\mathrm{NL}}$ they are stable and decay to zero (and the undeformed configuration is steady).

The deviation $G_4 - G_4^{\mathrm{NL}}$, for our numerical approximation to G_4^{NL}, is reported in figure 8 (top) as a function of the limiting perturbation $(\delta/R)_\infty^2$ and demonstrates the effect of nonlinearity on the critical value of G. The corresponding area deviation from the linear solution is shown in figure 8 (bottom).

Our results strongly suggest that for given l there exists a critical $G_l^{\mathrm{NL}} < G_l$ such that for $G = G_l^{\mathrm{NL}}$ a nonlinear, nontrivial steady shape exists. Thus, nonlinearity is destabilizing for the stationary shapes. This is in contrast with the results obtained in section 4.1 where nonlinearity stabilizes the pinchoff predicted by lin-

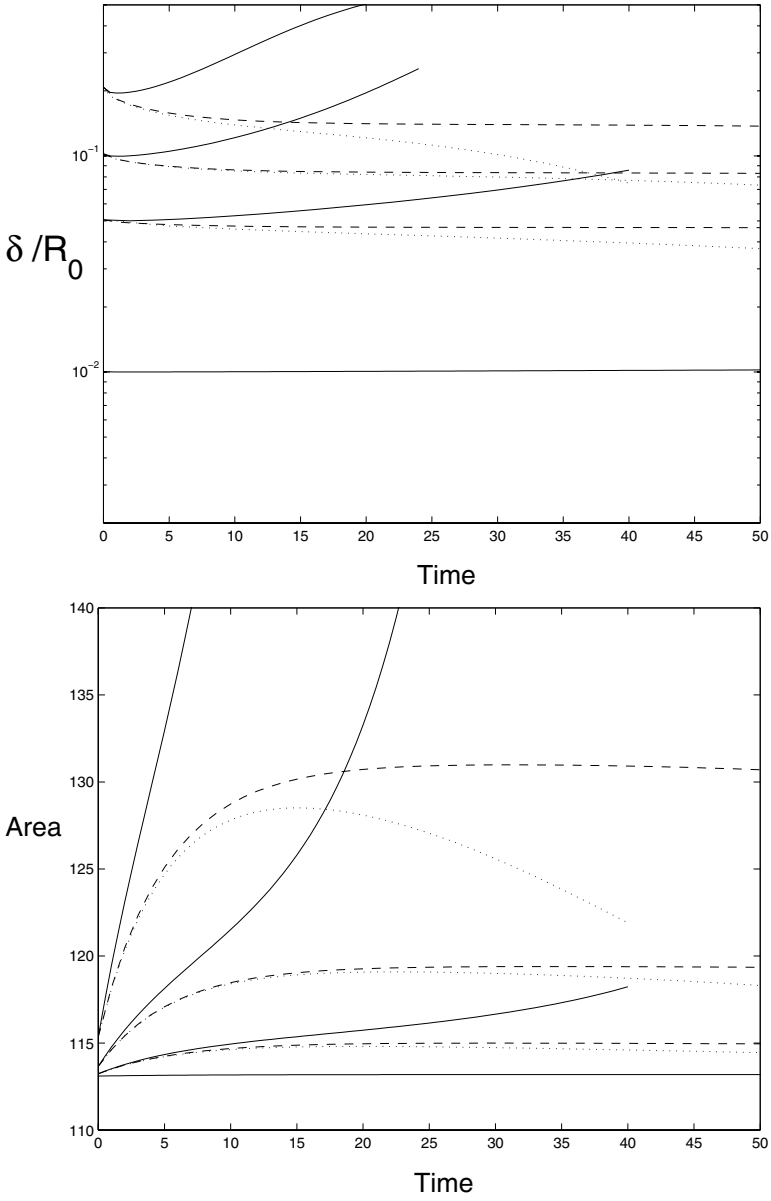

Fig. 7. Top: time evolution of the perturbation size relative to a spherical tumor for $d = 2$, different initial $l = 4$ perturbations and $A = 0.304$. Solid: $G = G_4$, Dotted: $G \ll G_4$, Dashed: $G \approx G_4^{\mathrm{NL}}$. Bottom: the corresponding evolution of the tumor area.

ear theory during unstable evolution. Finally, as expected, figure 8 indicates that the deviation of G_l^{NL} from the linear G_l is to the second order. For several perturbations examined, the initial (dashed curves) and steady nonlinear shapes (solid curves) are depicted in figure 9.

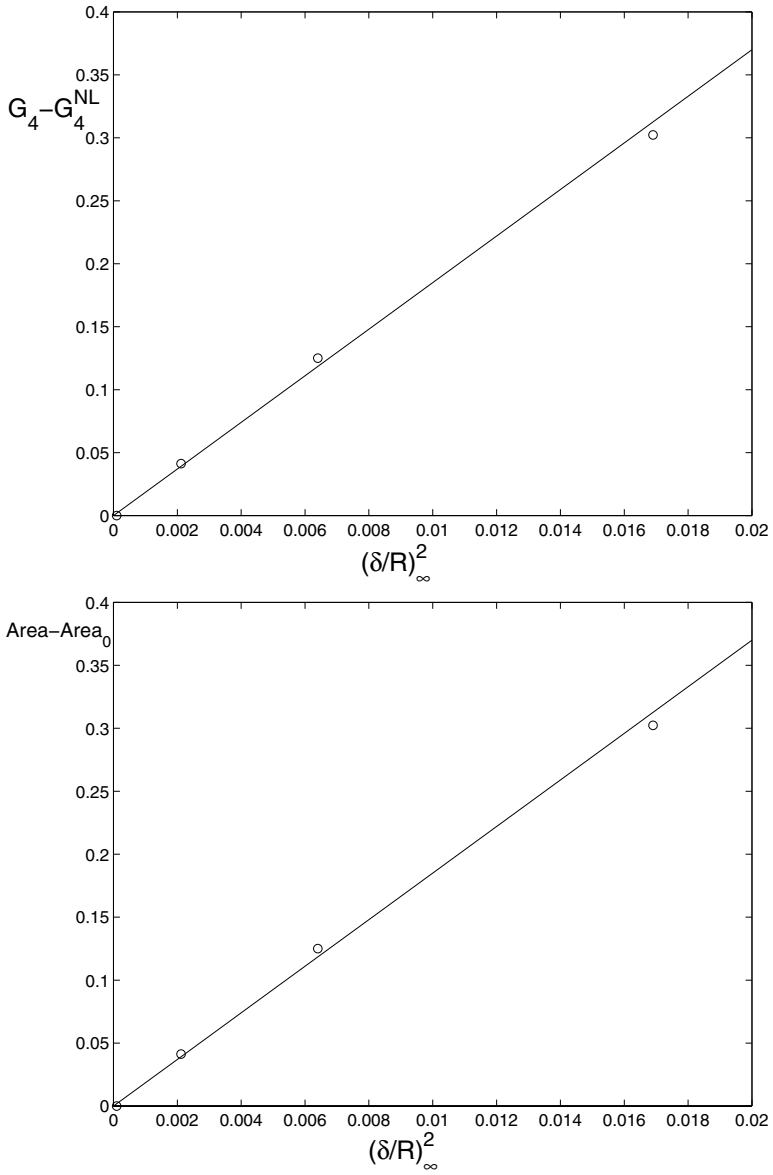

Fig. 8. Top: The difference $G_4 - G_4^{\mathrm{NL}}$ versus the limiting steady nonlinear perturbation size $(\delta/R)_\infty$. Bottom: The corresponding area difference.

4.3. Self-similar evolution

Here we study self-similar evolution using linear analysis and nonlinear simulations, and we explore the possibility of controlling the shape of a tumor during growth to take advantage of self-similar conditions and prevent growth of shape in-

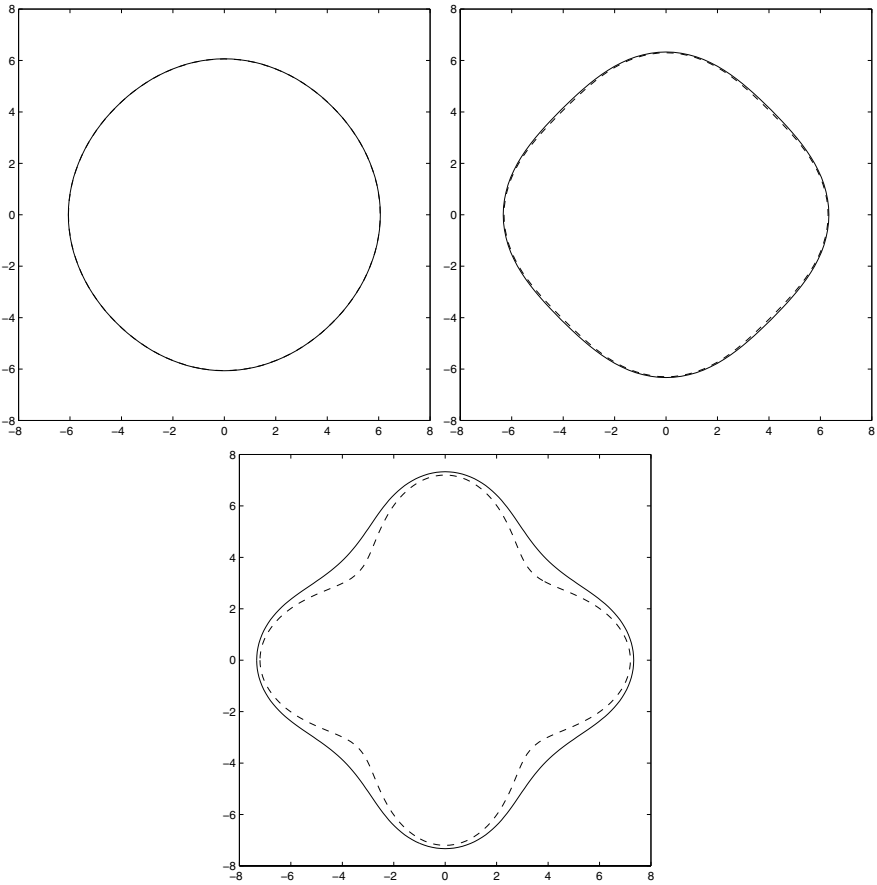

Fig. 9. The initial (dashed) and steady (solid) nonlinear tumor configurations for different initial perturbation amplitudes $\delta_0/R_0 = 0.01, 0.05, 0.2$ corresponding to the data in figure 7 with $G \approx G_4^{\mathrm{NL}}$.

stabilities. In figure 10 the evolution of a perturbation, predicted by linear analysis, during unbounded tumor growth ($R \to \infty$) is examined in the moderate-vascularization regime characterized by $G > 0$ and $A \leq 0$. As demonstrated from linear analysis in Sect. 2.3.1, corresponding to $d = 3$ (solid lines) and $A = A_l$ the shape tends to become self-similar. For $A > A_l$ the perturbation grows unbounded with respect to the unperturbed radius; for $A < A_l$ it decays to zero. For $d = 2$ (dashed lines) the perturbation always decays to zero. The behaviors as $R \to \infty$ are

$$\delta/R \sim \begin{cases} R^{-l}, & d = 2, \\ R^{-\left(3A^{-1}+l\right)}, & d = 3, \end{cases} \tag{39}$$

for $A \neq 0$, and

$$\delta/R \sim \begin{cases} R^{-1}, & d = 2, \\ \mathrm{e}^{R}, & d = 3, \end{cases} \tag{40}$$

independently of l, for $A = 0$. Note that in this case $V \to G$ for both $d = 2$ and 3.

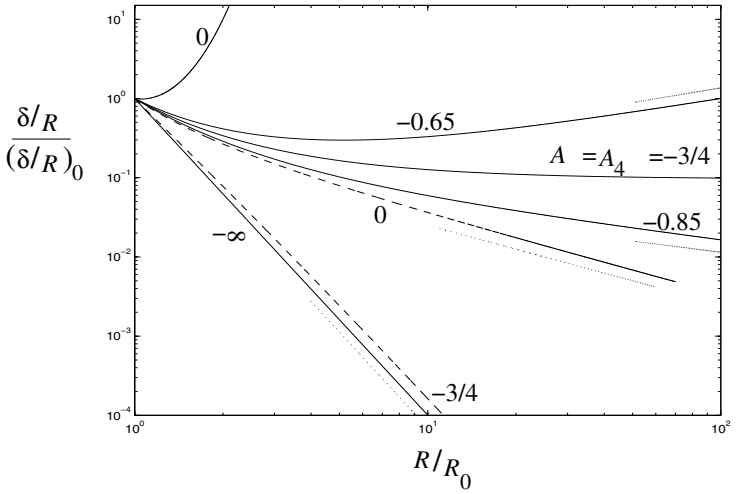

Fig. 10. Rescaled growth ratio $(\delta/R)\,/\,(\delta/R)_0$ as a function of rescaled radius R/R_0 during unbounded growth in the moderate-vascularization regime for $d = 2$ (dashed) and $d = 3$ (solid); $G = 1$, $l = 4$, and A as labeled. The initial radius $R_0 = 10$, except for the curve $d = 3$, $A = 0$, for which $R_0 = 7$. Asymptotic behaviors (dotted) from equations (39)–(40).

An analysis of the limit $(\delta/R)_\infty$ of the shape factor δ/R as $t \to \infty$ for $d = 3$ and $A = A_l = -3/l$ corresponding to self-similar evolution as $R \to \infty$ reveals that the nontrivial limiting shape factor $(\delta/R)_\infty \to (\delta/R)_0$ as $R_0 \to \infty$.

In the low-vascularization regime (G, $A > 0$) and in the high-vascularization regime ($G < 0$) with $A < 0$, no unbounded growth occurs. In these regimes the perturbation may either grow or decay, and thus complicated tumor morphologies can develop, as was illustrated by full nonlinear simulations in Sect. 4.1 in the low-vascularization regime.

4.3.1. Time-dependent parameters

In experiments of *in vitro* [35] and *in vivo* [33] growth, the time scales that characterize prevascular or moderately vascular growth are relatively short (e.g., one month) and apoptosis can be neglected [33], i.e. $\lambda_A = 0$. Thus the dimensionless parameter A becomes $A = -B/(1 - B)$. Therefore, it is possible to design an experiment where the parameter A may be varied by changing B (through nutrient concentrations in the blood, for example) while keeping the parameter G constant by adjusting the mitosis rate λ_M, for example through therapy. Analogously, it is also possible to vary G while maintaining A constant. On longer time scales, apoptosis is nonzero, and can be also controlled through therapy (e.g., radiation). These considerations and the following analysis reveal that, by varying the parameters appropriately, it should be possible to control the shapes of growing tumors thereby preventing the occurence of instabilities and invasive fingering.

One example of shape control is to maintain self-similar evolution during growth by setting $\frac{\mathrm{d}}{\mathrm{d}t}(\delta/R) = 0$ identically in equation (13). This can be achieved by keeping G constant and varying A as a function of the unperturbed radius R by

$$A = \begin{cases} \dfrac{2\left(l^2-1\right)}{G\,R^3} + 2l^{-1}\left(\dfrac{I_1(R)\;I_{l-1}(R)}{I_0(R)\;I_l(R)} - 1\right) \\ \qquad -2\left(1-2l^{-1}\right)\;R^{-1}\;I_1(R)/I_0(R), \qquad d=2, \\ \dfrac{3(l+2)(l-1)}{G\,R^3} - 3l^{-1} \\ \qquad +3\left(1+3l^{-1}\right)\;R^{-2}\;(R/\tanh(R)-1), \qquad d=3. \end{cases} \tag{41}$$

In figure 11 (top) the apoptosis parameter $A(R)$ from Eq. (41) is shown for $d = 2$ (dashed lines) and $d = 3$ (solid). The growth velocity corresponding to self-similar evolution, obtained from (7) with A given by (41), is plotted in figure 11 (bottom). The curves of A divide the plot into regions of stable growth and regions of unstable growth of a given mode l. Figures 11 top and bottom indicate that in the low-vascularization (diffusion-dominated) regime ($G > 0$, $A > 0$) self-similar evolution towards a stationary state is not possible for G constant (the stationary states R_∞ correspond to the intersection of curves (41) in figure 11 (top) with the curves describing stationary radii). For instance, the growth velocity $V < 0$ for initial radius $R_0 < R_\infty$, and thus self-similar shrinkage of the tumor to zero occurs. On the other hand, for $R_0 > R_\infty$, $V > 0$, and thus self-similar growth away from the stationary radius occurs. In the high-vascularization regime ($G < 0$), during self-similar evolution the velocity $V < 0$. Thus self-similar shrinkage of a tumor from arbitrary initial condition to a point occurs, and self-similar unbounded growth is not possible.

Let us now focus on unbounded growth conditions: $AG < 0$. The limiting behaviors as $R \to \infty$ are $A \approx 2l^{-1}R^{-1} > 0$ for $d = 2$, and $A \approx -3l^{-1} + 3\left(1+3l^{-1}\right)R^{-1} < 0$ for $d = 3$, and are independent of G. For $G > 0$ and $A < 0$ (moderate-vascularization regime), growth is stable for $A < A(R)$ and unstable otherwise (note that $A < A(R)$ always for $d = 2$); for $G < 0$ and $A > 0$ (high vascularization), growth is always stable since the stability condition is in this case $A > A(R)$ and $A(R) < 0$ as $R \to \infty$. For $d = 2$, self-similar evolution remains in the low-vascularization regime ($A > 0$), and does not occur in the moderate-vascularization regime; in contrast, for $d = 3$, a transition takes place into the moderate-vascularization regime (A becomes negative), and leads to unbounded self-similar growth. One can imagine an experiment in which an initially avascular tumor grows in the diffusion-dominated regime with $G > 0$ and $A = 0$. This corresponds to moving along the zero axis to the right, in figure 11, as illustrated by the open circles. As the tumor grows by diffusion, angiogenesis occurs, and A becomes negative. By adjusting A through the concentration of nutrient in the blood stream, while keeping G constant by adjusting the mitosis rate λ_M at the same time, one

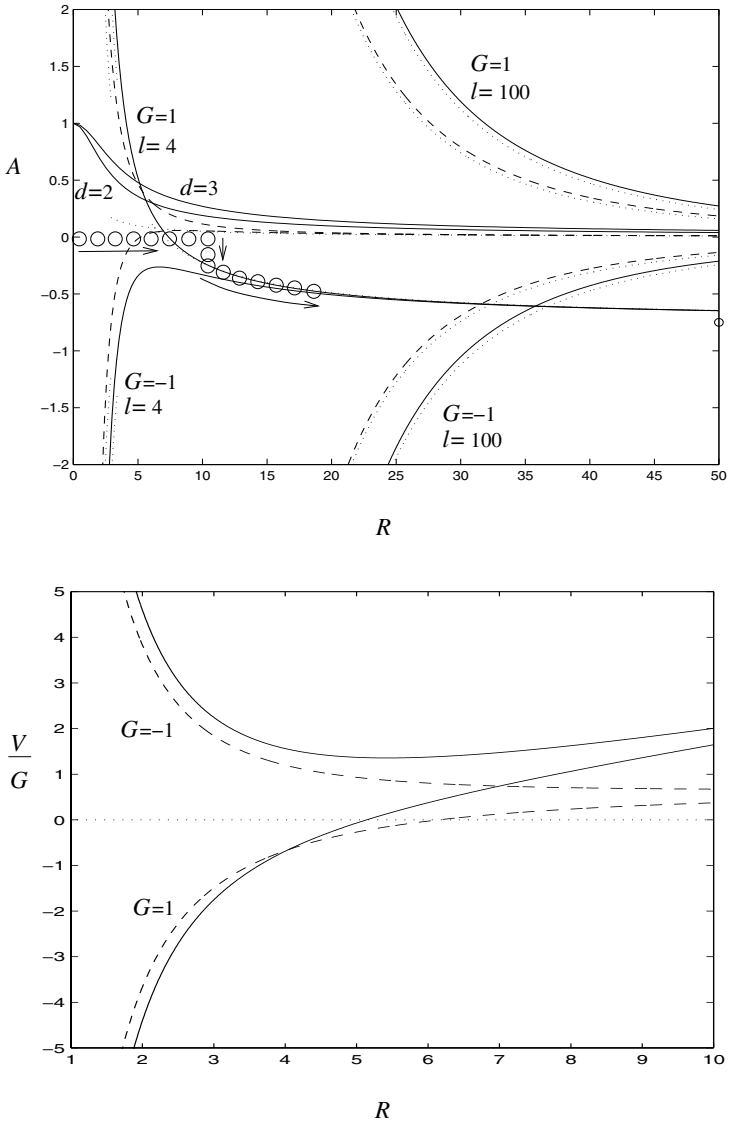

Fig. 11. Top: apoptosis parameter A as a function of unperturbed radius R from condition (41) for self-similar evolution; $d = 2$ (dashed) and $d = 3$ (solid); G and l labelled. Asymptotic behaviors (42) (dotted). The two solid curves labelled with values of d correspond to stationary radii. Bottom: corresponding growth velocity $G^{-1}V$ for $l = 4$.

can evolve the vascularized tumor along the curve $A(R)$ that corresponds to self-similar growth in the moderate-vascularization regime, thus controlling the shape and preventing invasive fingering. Correspondingly, the proliferation rate should be varied as: $(\lambda_M - \lambda_A)/\lambda_R = G\,(1 - A(R))$. As $l \to \infty$,

$$A \to \begin{cases} 2\left(l^2 - 1\right)\ G^{-1}R^{-3}, & d = 2, \\ 3\,(l+2)\,(l-1)\ G^{-1}R^{-3}, & d = 3, \end{cases} \tag{42}$$

and thus $A > 0$ and self-similar evolution in the low-vascularization regime becomes possible at all radii (and it becomes forbidden in the moderate-vascularization regime) also for $d = 3$.

The apoptosis parameter for self-similar evolution with $d = 1$ is $A = \left(G^{-1}l^3 - 1 + \left(l^2+1\right)^{\frac{1}{2}}\right)(lR-1)^{-1}$; note as a special case that, for $G = l^{-3}\left(\left(1+l^2\right)^{\frac{1}{2}} - 1\right)$, $A = 0$ and unbounded self-similar growth occurs with constant parameters. The behaviors described remain qualitatively unchanged for different values of l.

To summarize, we found self-similar evolution, with the possiblity of shape control, in all regimes with varying A and constant G. However, we discovered that in the low-vascularization regime, self-similar evolution to a steady state does not occur under these conditions. Similarly, self-similar unbounded growth in the high-vascularization regime does not occur. In Appendix B we examine the possibility of self-similar evolution to a steady-state in the low-vascularization regime and of unbounded self-similar growth in the high vascularization regime by varying G in addition to A.

4.3.2. Effect of nonlinearity

We now investigate the effect of nonlinearity on the self-similar evolution for $d = 2$ predicted by the linear analysis. As discussed in section 4.3.1, self-similar evolution requires the time-dependent apoptosis parameter $A = A(l, G, R)$ given in Eq. (41) and plotted in figure 11 (top). The radius R, used in the nonlinear simulation, is determined by the area of an equivalent circle: $R = \sqrt{H/\pi}$. Examples of nonlinear self-similar evolution in the low-vascularization regime with $l = 4$ and $G = 1$ are shown in figure 12. In the top graph, the initial radius and perturbation are $R_0 = 7$ and $\delta_0 = 0.3$. Since the velocity $V > 0$, from figure 11 (bottom), the tumor grows and correspondingly A decreases. In the bottom graph, $R_0 = 4$ and $\delta_0 = 0.2$; the corresponding $V < 0$ indicating that the tumor shrinks (A increases). The solid curves correspond to the nonlinear solution, at time $t = 0$ and at a later time, and the dashed curves to the linear. The two are nearly indistinguishable revealing that self-similar evolution is robust to nonlinearity for small perturbations.

In figure 13, the linear and nonlinear solutions are compared in the low-vascularization regime for $l = 5$, $G = 1$, $A = A(l, G, R)$ and $R_0 = 4$. Since $V < 0$, the tumors shrink and A increases. In the top figure, $\delta_0 = 0.2$ and in the bottom $\delta_0 = 0.4$. The results reveal that large perburbations are nonlinearly unstable and grow, leading to a topological transition. In the last frame in figure 13 (bottom), the

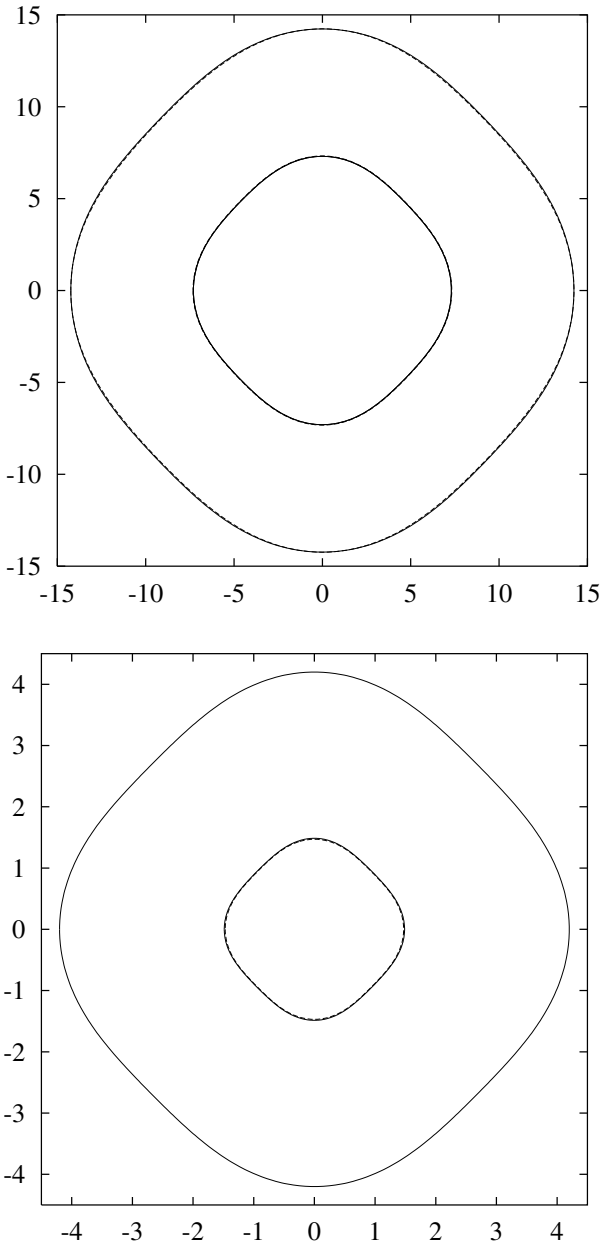

Fig. 12. Top: self-similar nonlinear growth for $R_0 = 7$ and $\delta_0 = 0.3$ (times $t = 0$ and $t = 20$ shown). Bottom: self-similar nonlinear shrinkage for $R_0 = 4$ and $\delta_0 = 0.2$ ($t = 0$ and $t = 1.6$ shown). The solid curves correspond to the nonlinear solution and the dashed curves to the linear. In both cases, the evolution is in the low-vascularization regime with $d = 2$, $l = 4$ and $G = 1$, and the time-dependent $A = A(l, G, R)$ given in Eq. (41) and plotted in figure 11 (top).

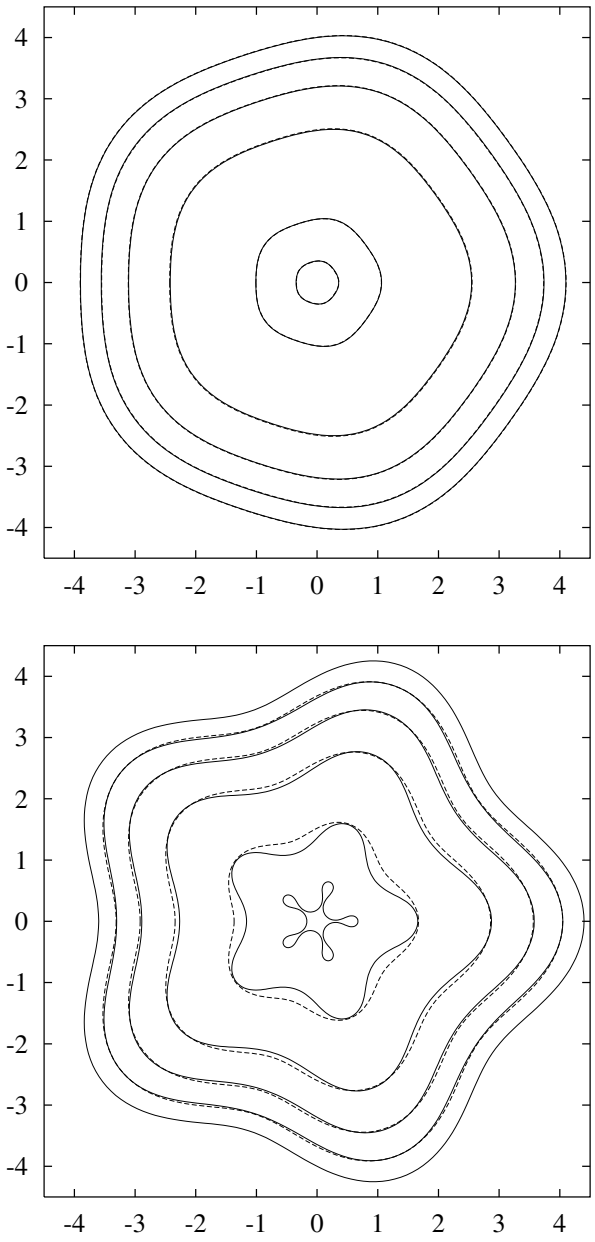

Fig. 13. Top: self-similar shrinkage for $R_0 = 4$ and $\delta_0 = 0.2$ ($t = 0$ to 0.96 shown). Bottom: Unstable shrinkage for $R_0 = 4$ and $\delta_0 = 0.4$ ($t = 0$ to 0.99). The solid curves correspond to the nonlinear solution and the dashed curves to the linear. In both cases, $d = 2$, $G = 1$, $l = 5$ and the evolution is in the low-vascularization regime. $A = A(l, G, R)$ given in Eq. (41) and plotted in figure 11 (top).

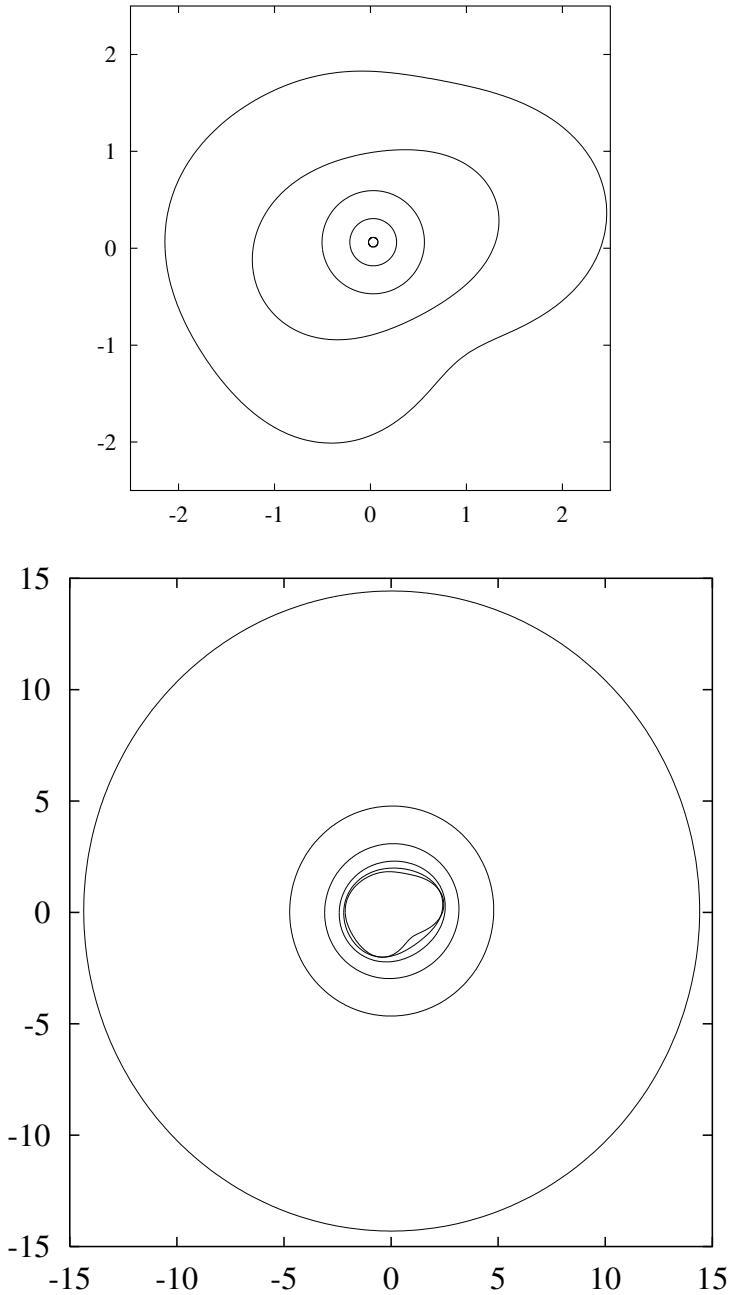

Fig. 14. Nonlinear stable evolution in the high vascularization regime. Top: shrinkage with $A = 0.2$ and $G = -5$ ($t = 0$, 0.4, 0.8, 1.2 and 2.0 shown). Bottom: growth with $A = 0.8$ and $G = -5$ ($t = 0$, 0.2, 0.5, 1.0, 1.5 and 2.3 shown). In both, the initial data is as in Eq. (36).

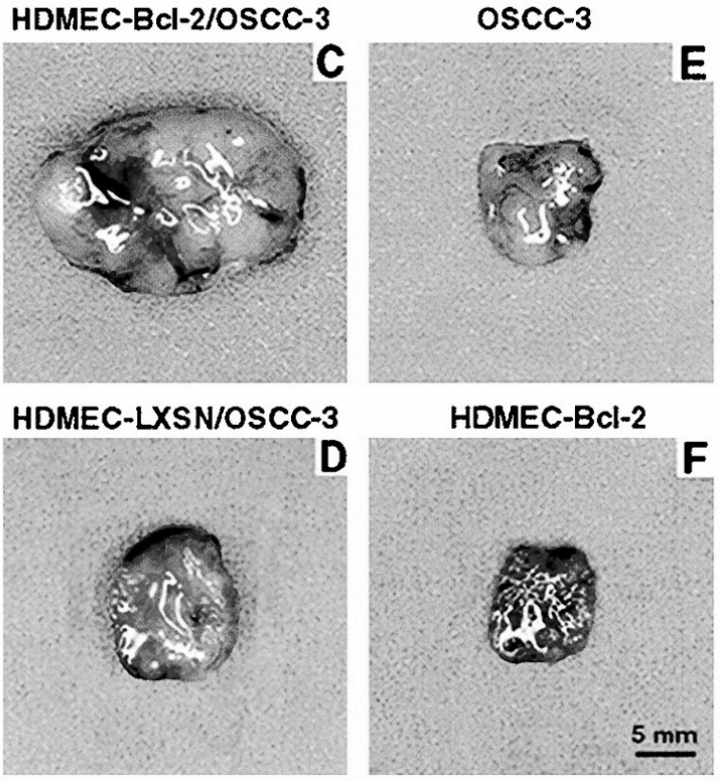

Fig. 15. HDMEC tumors seeded in biodegradable sponges and implanted in SCID mice from [30]. The larger tumors overexpress the angiogenic factor Bcl-2 and are thus more highly vascularized.

onset of pinch-off is evident. This can have important implications for therapy. For example, one can imagine an experiment in which a tumor is made to shrink by therapy such that A is increased by increasing the apoptosis rate λ_A. Our example shows that a rapid decrease in size can result in shape instability leading to tumor break-up and the formation of microscopic tumor fragments that can enter the blood stream through leaky blood vessels thus leading to metastases.

4.4. Evolution in the high vascularization regime

In the high-vascularization regime ($G < 0$), both shrinkage and growth of tumors occur. Shrinkage ($A < 0$) may be stable, self-similar and unstable. In contrast, unbounded growth ($A > 0$) is always characterized by a decay of the perturbation to zero with respect to the unperturbed radius and is thus stable for both $d = 2$ and 3. In the nonlinear regime, we find that self-similar and unstable shrinkage are qualitatively very similar to that presented in figure 13 and therefore we do not present these results here. Instead, we present stable, nonlinear evolution from the

multimodal initial data given in Eq. (36) with $G = -5$. In figure 14 (top), the stable shrinkage of a tumor is shown with $A = 0.2$. In the bottom graph, there is less apoptosis, $A = 0.8$, and unbounded, stable growth occurs. In fact, all the nonlinear simulations of growth we have performed in the high vascularization regime lead to stable evolution, in agreement with the linear analysis.

In contrast, it is known experimentally that highly vascularized *carcinoma* evolve invasively by extending branches into regions of the external tissue where the mechanical resistance is lowest (e.g. [9]). Thus our results suggest that the formation of invasive tumors should be due to anisotropies rather than to vascularization alone. Anisotropies (e.g., in the distribution of the resistance of the external tissue to tumor growth, or in the distribution of blood vessels) have been neglected in the model studied here. This conclusion has not been recognized before and is supported by recent experiments [30] of *in vivo* angiogenesis and tumor growth, in which stable growth is observed of highly vascularized tumors that have been embedded in an isotropic, biodegradable sponge-like material and then implanted in mice. Examples of four such tumors are shown in figure 15 (from Ref. [30]). Because of the isotropy of the sponge, the tumor/tissue blood-vessel distribution is isotropic as is assumed in the model studied here, and during growth the tumors maintain a compact, roughly spheroidal shape.

5. Conclusions

We have studied solid tumor growth in the nonlinear regime using boundary-integral simulations. In the model investigated [18,24,8,3], the tumor core is assumed to be nonnecrotic and no inhibitor chemical species to be present. We have developed a new formulation of this classical model and we have demonstrated that tumor evolution is described by a reduced set of two dimensionless parameters and is qualitatively unaffected by the number of spatial dimensions. The parameter G describes the relative rate of mitosis to the relaxation mechanisms. The parameter A describes the balance between apoptosis and mitosis. Both parameters also include the effect of vascularization.

Our analysis and nonlinear simulations have revealed that the two new dimensionless groups uniquely subdivide tumor growth into three regimes associated with increasing degrees of vascularization: low (diffusion dominated, e.g., *in vitro*), moderate and high vascularization, that correspond to the regimes observed in *in vivo* experiments. We have demonstrated, by constructing explicit examples using nonlinear simulations, that critical conditions exist for which the tumor evolves to nontrivial dormant states or grows self-similarly in the first two regimes. Self-similar growth separates stable tumors, that grow maintaining a compact shape, from unstable tumors, for which vascularization is favored and growth leads to invasive fingering into the healthy tissues. We have illustrated the possibility of tumor shape control during growth by simulating a physical experiment in which the dimensionless parameters A and G are varied in time (for example by changing the physical parameters through therapy) to maintain stable or self-similar growth conditions thus preventing invasive growth and hampering angiogenesis. We have also shown that nonlinear unstable growth may lead to topological transi-

tions such as tumor breakup and reconnection with encapsulation of healthy tissue. Interestingly we have found that for highly vascularized tumors, while they grow unbounded, their shape always stays compact and invasive fingering does not occur. This is in agreement with recent experimental observations [30] of *in vivo* tumor growth, and suggests that the invasive growth of highly-vascularized tumors is associated to vascular and elastic anisotropies, which are not included in the model we have studied.

The work presented here demonstrates that nonlinear simulations are a powerful tool for understanding the phenomena that lead to growth of tumors. We are working at the development of a three-dimensional computer simulator of a more sophisticated model of tumor growth, that includes the direct description of angiogenesis, and the effects of vascular and elastic (e.g., [20]) anisotropies that may set preferred directions of growth and thus should be responsible for the invasive growth of maligant tumors. Angiogenesis is described by following the diffusion of tumor angiogenic factors through the tissues, and the chemotaxis of endothelial cells in response, leading to a nonuniform density of blood vessels. Such a sophisticated computer simulator should be useful for the scientific understanding of the conditions under which complex tumor morphologies develop during growth (such as networks of blood vessels and shape instabilities), and also to help the design of targeted physical experiments *in vitro* or *in vivo*. Finally, this cancer simulator should find applications in a clinic environment, for example for testing different candidate therapies. As was only qualitatively illustrated in this paper, therapy will be simulated by rigorously describing its effect on the physical parameters (such as mitosis and death rates) that characterize a tumor's microenvironment. Simulations of a specific patient's reaction to each therapy can thus lead to the selection of the most promising therapies to be applied *in vivo*.

Appendix A

Governing equations

We consider a nonnecrotic tumor occupying a volume $\Omega(t)$. In the absence of inhibitor chemical species, following [18,7,14], the quasi-steady diffusion equation for the concentration $\sigma(\mathbf{x}, t)$ of nutrient is

$$0 = D\nabla^2\sigma + \Gamma, \tag{43}$$

where D is the diffusion constant, and Γ is the rate at which nutrient is added to Ω. The assumption of quasi-steady diffusion [7] is well supported by the consideration that the tumor volume doubling time scale (e.g., one day) is typically much larger that the diffusion time scale ($\approx$ one minute).

The rate Γ incorporates all sources and sinks of nutrient in the tumor volume. Nutrient is supplied by the vasculature at a rate $\Gamma_B(\sigma, \sigma_B)$, where σ_B is the (uniform) concentration in the blood. The rate of consumption of nutrient by the tumor cells is $\lambda\,\sigma$, with λ uniform. The blood-tissue transfer rate is assumed to be linear:

$$\Gamma_B = -\lambda_B\ (\sigma - \sigma_B)\,, \tag{44}$$

where λ_B is uniform. Thus, the rate Γ is given by

$$\Gamma = -\lambda_B \ (\sigma - \sigma_B) - \lambda \, \sigma. \tag{45}$$

Modeling the tumor as an incompressible fluid, it follows that the velocity field $\mathbf{u}$ in Ω satisfies the continuity equation

$$\nabla \cdot \mathbf{u} = \lambda_P, \tag{46}$$

where λ_P is the cell-proliferation rate. We choose here the model

$$\lambda_P = b\sigma - \lambda_A, \tag{47}$$

which is linear with respect to the nutrient concentration [7]: λ_A is the rate of apoptosis and b and λ_A are assumed to be uniform.

The velocity is assumed to obey Darcy's law [17]:

$$\mathbf{u} = -\mu \nabla P, \tag{48}$$

where μ is the (constant) cell mobility and $P(\mathbf{x}, t)$ is the pressure inside Ω.

The boundary condition for concentration at $\Sigma \equiv \partial\Omega$ is

$$(\sigma)_\Sigma = \sigma^\infty, \tag{49}$$

where σ^∞ is the nutrient concentration outside the tumor volume, assumed to be uniform. This sets the characteristic mitosis rate to be

$$\lambda_M = b\sigma^\infty.$$

Pressure is assumed to satisfy the Laplace-Young boundary condition

$$(P)_\Sigma = \gamma\kappa, \tag{50}$$

where γ is the surface tension related to cell-to-cell adhesive forces, and κ is local total curvature. Finally, the normal velocity $V = \mathbf{n} \cdot (\mathbf{u})_\Sigma$ at the tumor boundary (with outward normal $\mathbf{n}$) is

$$V = -\mu \, \mathbf{n} \cdot (\nabla P)_\Sigma \, . \tag{51}$$

Dimensionless formulation

Equations (43) and (45) reveal that there is an intrinsic length scale

$$L_D = D^{\frac{1}{2}} \, (\lambda_B + \lambda)^{-\frac{1}{2}} \, , \tag{52}$$

which for $\lambda_B = 0$ roughly estimates the stable size of an avascular tumor when diffusion of nutrient and consumption balance. By nondimensionalizing lengths with L_D we obtain, from equations (48) and (50), an intrinsic relaxation time scale λ_R^{-1} corresponding to the rate

$$\lambda_R = \mu\gamma L_D^{-3} \tag{53}$$

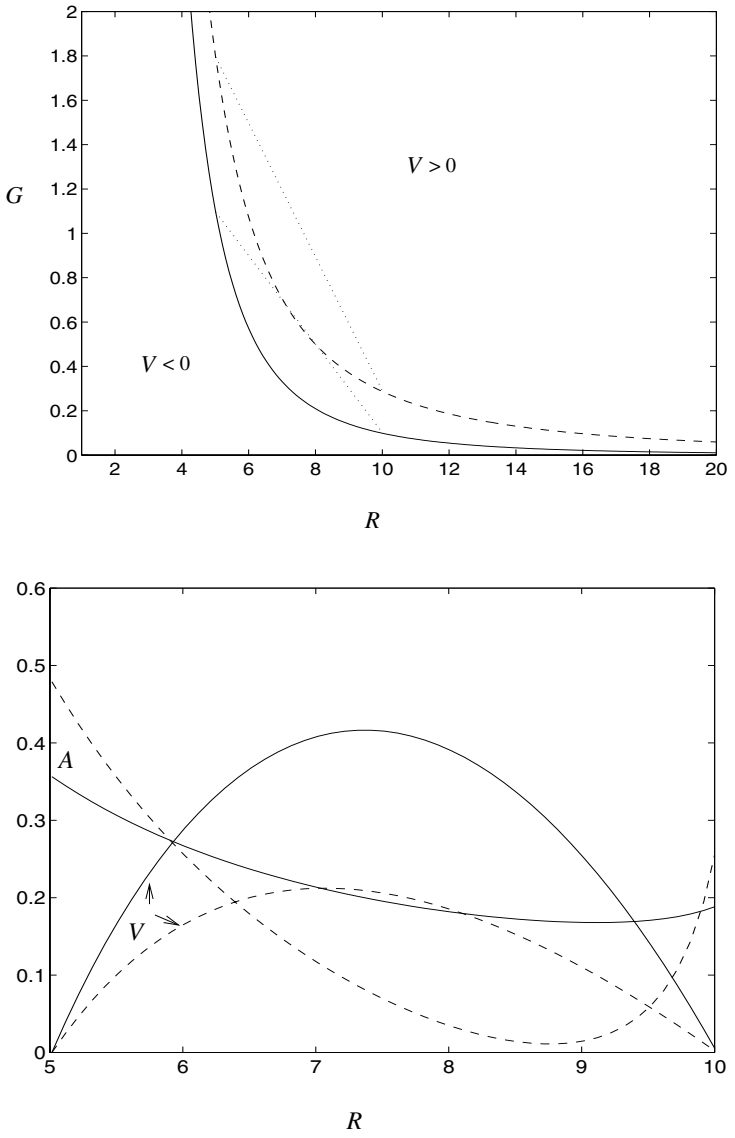

Fig. 16. Top: growth parameter G from condition (41) for shape invariance, with $V = 0$ and $A(R)$ from Eq. (7) as a function of radius R; $d = 2$ (dashed) and $d = 3$ (solid); $l = 4$. Experiment of self-similar evolution between stationary states (dotted), with G imposed as a linear function of R. Bottom: apoptosis parameter A from (41), and growth velocity V, as a function of radius R during such experiment.

associated to the relaxation mechanisms cell mobility and surface tension. The above rate is used to nondimensionalize time.

Let us introduce the dimensionless parameters A and G defined in (4) and the modified concentration and pressure $\bar{\Gamma}$ and $\bar{p}$ so that

$$\sigma = \sigma^{\infty}\left(1-(1-B)\left(1-\bar{\Gamma}\right)\right),$$
$$P = \frac{\gamma}{L_D}\left(\bar{p}+\left(1-\bar{\Gamma}\right)\,G + A\,G\,\frac{\mathbf{x}\cdot\mathbf{x}}{2d}\right). \tag{54}$$

The parameter

$$B = \frac{\sigma_B}{\sigma^{\infty}}\frac{\lambda_B}{\lambda_B+\lambda} \tag{55}$$

represents the extent of vascularization.

By algebraic manipulations it can be shown that equations (1) is obtained from equations (43), (45) and (49). Equations (2) are obtained from (46)–(48) and (50). Finally, equation (3) is obtained from (51). In the main text of the paper, the bars have been dropped for simplicity.

Appendix B

Here we examine the possibility of self-similar evolution to a steady-state in the low-vascularization regime and of unbounded self-similar growth in the high vascularization regime by varying G in addition to A. In figure 16 (top) the values of growth parameter G as a function of radius R are plotted corresponding to nontrivial stationary states with a fixed tumor shape: $\frac{\mathrm{d}}{\mathrm{d}R}\,(\delta/R) = 0$. In the high-vascularization regime ($G < 0$), self-similar evolution occurs below the curves $V = 0$ in figure 16 (top), and thus $V < 0$ and self-similar unbounded growth remains forbidden. Thus, unbounded growth in the high-vascularization is always stable even for variable A and G which is in agreement with recent experiments [30].

We consider then self-similar evolution between nontrivial stationary states in the low-vascularization regime ($G > 0$). The dotted lines in figure 16 (top) represent an experiment in which G is varied linearly between a stationary state $R_{\infty,1}$ and a stationary state $R_{\infty,2} > R_{\infty,1}$. In figure 16 (bottom), the corresponding growth velocities and time-dependent apoptosis parameters are shown. The figure reveals that during this experiment the growth velocity $V > 0$ and thus self-similar evolution is possible between the two stationary states. Other experimental paths are possible, that lead to either growth or shrinkage of tumors to stationary states. The qualitative behaviors described are not affected by l.

Acknowledgements. V. Cristini and J. Lowengrub acknowledge Professor S. Ramakrishnan at the University of Minnesota for useful discussions, partial support from the National Science Foundation and the Minnesota Supercomputing Institute, and the hospitality of the Institute for Mathematics and its Applications. V. Cristini also acknowledges the support of the MSI through a Reseach Scholar Award. Q. Nie acknowledges partial support from the NSF.

References

1. Adam, J.: General Aspects of Modeling Tumor Growth and Immune Response. *In: A Survey of Models on Tumor Immune Systems Dynamics, J. Adam and N. Bellomo Editors* (Birkhauser, Boston 1996) 15–87
2. Bellomo, N., Preziosi, L.: Modelling and Mathematical Problems Related to Tumor Evolution and Its Interaction with the Immune System. Mathl. Comput. Modelling **32**, 413–452 (2000)
3. Byrne, H.M.: The importance of intercellular adhesion in the development of carcinomas. IMA J. Math. Med. Biol. **14**, 305–323 (1997)
4. Byrne, H.M.: A weakly nonlinear analysis of a model of avascular solid tumour growth. J. Math. Biol. **39**, 59–89 (1999)
5. Byrne, H.M., Chaplain, M.A.J.: Free boundary value problems associated with the growth and development of multicellular spheroids. Eur. J. Appl. Math. **8**, 639–658 (1997)
6. Byrne, H.M., Chaplain, M.A.J.: Growth of Nonnecrotic Tumors in the Presence and Absence of Inhibitors. Mathl. Biosci. **135**, 187–216 (1996)
7. Byrne, H.M., Chaplain, M.A.J.: Growth of Nonnecrotic Tumors in the Presence and Absence of Inhibitors. Mathl. Biosci. **130**, 151–181 (1995)
8. Byrne, H.M., Chaplain, M.A.J.: Modelling the role of cell-cell adhesion in the growth and development of carcinomas. Mathl. Comput. Modelling **24**, 1–17 (1996)
9. Chaplain, M.A.J.: Avascular growth, Angiogenesis and Vascular growth in Solid Tumours: The Mathematic Modelling of the Stages of Tumour Development. Mathl. Comput. Modelling **23**, 47–87 (1996)
10. Colton, D., Kress, R.: *Integral Equation Methods in Scattering Theory* (Wiley-Interscience, New York 1983)
11. Colton, D., Kress, R.: *Inverse Acroustic and Electromagnetic Scattering Theory* (Springer, Berlin 1992)
12. Cristini, V., Lowengrub, J.: Three-dimensional crystal growth. I. Linear analysis and self-similar evolution. J. Crystal Growth **240**, 267–276 (2002)
13. Friedman, A., Reitich, F.: On the existence of spatially patterned dormant malignancies in a model for the growth of non-necrotic vascular tumors. Math. Models Meth. Appl. Sci. **11**, 601–625 (2001)
14. Friedman, A., Reitich, F.: Analysis of a mathematical model for the growth of tumors. J. Math. Biol. **38**, 262 (1999)
15. Greenbaum, A., Greengard, L., McFadden, G.B.: Laplace's equation and the Dirichlet-Neumann map in multiply connected domains, J. Comp. Phys. **105**, 267 (1993)
16. Greenbaum, A., Greengard, L., McFadden, G.B.: On the numerical solution of a hypersingular integral equation in scattering theory, J. Comp. Appl. Math. **61**, 345–360 (1995)
17. Greenspan, H.P.: Models for the Growth of a Solid Tumor by diffusion. Stud. Appl. Math. **LI,4**, 317–340 (1972)
18. Greenspan, H.P.: On the growth and stability of cell cultures and solid tumors. J. Theor. Biol. **56**, 229–242 (1976)
19. Kansal, A.A., Torquato, S., Harsh IV, G.R., Chiocca, E.A., Deisboeck, T.S: Simulated brain tumor growth dynamics using a 3-D cellular automaton, J. Theor. Biol. **203**, 367–382 (2000)
20. Jones, A.F., Byrne, H.M., Gibson, J.S., Dold, J.W.: A mathematical model of the stress induced during avascular tumour growth. J. Math. Biol. **40**, 473–499 (2000)
21. Leo, P., Lowengrub, J., Nie, Q. Microstructural Evolution in Orthotropic Elastic Media, J. Comp. Phys. **157**, 44–88 (2000)
22. Maue, A.: Uber die Formulierung eines allgemeinen Beugungsproblems durch eine Integralgleichung, Zeit. Physik **126**, 601–608 (1949)

23. Martensen, E.: Uber die Methode zum raumlichen Neumannschen Problem mit einer Anwendung fur torusartige Berandungen, Acta Math **109**, 75–135 (1963)
24. McElwain, D.L.S., Morris, L.E.: Apoptosis as a volume loss mechanism in mathematical models of solid tumor growth. Math. Biosci. **39**, 147–157 (1978)
25. Mikhlin, S.G.: *Integral Equations and Their Applications to Certain Problems in Mechanics, Mathematical Physics, and Technology* (Pergamon Press, New York 1957)
26. Mueller-Klieser, W.: Multicellular spheroids: a review on cellular aggregates in cancer research. J. Cancer Res. Clin. Oncol. **113**, 101–122 (1987)
27. Netti, P.A.: University of naples, Italy. Personal communication
28. Netti, P.A., Baxter, L.T., Boucher, Y., Skalak, R., Jain, R.K.: Time dependent behavior of interstitial fluid pressure in solid tumors: Implications for drug delivery. Cancer Res. **55**, 5451–5458 (1995)
29. Please, C.P., Pettet, G., McElwain, D.L.S.: A new approach to modeling the formation of necrotic regions in tumors. Appl. Math. Lett. **11**, 89–94 (1998)
30. Nor, J.E., Christensen, J., Liu, J., Peters, M., Mooney, D.J., Strieter, R.M., Polverini, P.J.: Up-Regulation of Bcl-2 in Microvascular Endothelial Cells Enhances Intratumoral Angiogenesis and Accelerates Tumor Growth. Cancer Res. **61**, 2183–2188 (2001)
31. Youcef Saad, Martin H., Schultz, GMRES: A Generalized Minimal Residual Algorithm for Nonsymmetric Linear Systems, SIAM J. Sci. Stat. Comput. **7**, 856 (1986)
32. Hou, T., Lowengrub, J., Shelley, M.: Removing the Stiffness from Interfacial Flows with Surface Tension, J. Comp. Phys. **114**, 312–338 (1994)
33. Ramakrishnan, S.: Department of Pharmacology, University of Minnesota. Personal communication
34. Sidi, A., Israeli, M.: Quadrature Methods for Singular and Weakly Fredholm Integral Equations, J. Sci. Comput. **3**, 201–231 (1988)
35. Sutherland, R.M.: Cell and Environment interactions in tumor microregions: the multicell spheroid model. Science **240**, 177–184 (1988)